AGU PUBLICATIONS

JGR

Journal of Geophysical Research: Biogeosciences

RESEARCH ARTICLE
10.1002/2016JG003660

Special Section:
Atmosphere-ice-ocean-ecosystem processes in a thinner Arctic sea ice regime: the Norwegian young sea ICE cruise 2015 (N-ICE2015)

Sea ice thermohaline dynamics and biogeochemistry in the Arctic Ocean: Empirical and model results

Pedro Duarte[1], Amelie Meyer[1], Lasse M. Olsen[1], Hanna M. Kauko[1,2], Philipp Assmy[1], Anja Rösel[1], Polona Itkin[1], Stephen R. Hudson[1], Mats A. Granskog[1], Sebastian Gerland[1], Arild Sundfjord[1], Harald Steen[1], Haakon Hop[1,3], Lana Cohen[1], Algot K. Peterson[4], Nicole Jeffery[5], Scott M. Elliott[5], Elizabeth C. Hunke[6], and Adrian K. Turner[6]

[1]Norwegian Polar Institute, Tromsø, Norway, [2]Centre for Autonomous Marine Operations and Systems, Department of Biology, Norwegian University of Science and Technology, Trondheim, Norway, [3]Department of Arctic and Marine Biology, Faculty of Biosciences, Fisheries and Economics, UiT The Arctic University of Norway, Tromsø, Norway, [4]Geophysical Institute, Bjerknes Centre for Climate Research, University in Bergen, Bergen, Norway, [5]Computer, Computational and Statistical Sciences Division, Los Alamos National Laboratory, Los Alamos, New Mexico, USA, [6]Theoretical Division, Los Alamos National Laboratory, Los Alamos, New Mexico, USA

Key Points:
- Sea ice physical variables can be accurately simulated at time scales of 2 months using a 1-D vertically resolved state of the art model
- Ice algal motility driven by gradients in limiting factors is a plausible mechanism to explain their vertical distribution
- The predictable increase in the area of refrozen leads may have a negative effect on vertically integrated ice algal primary production

Supporting Information:
- Supporting Information S1

Correspondence to:
P. Duarte,
pedro.duarte@npolar.no

Citation:
Duarte, P., et al. (2017), Sea ice thermohaline dynamics and biogeochemistry in the Arctic Ocean: Empirical and model results, *J. Geophys. Res. Biogeosci.*, *122*, 1632–1654, doi:10.1002/2016JG003660.

Received 6 OCT 2016
Accepted 15 MAY 2017
Accepted article online 8 JUN 2017
Published online 11 JUL 2017

Abstract Large changes in the sea ice regime of the Arctic Ocean have occurred over the last decades justifying the development of models to forecast sea ice physics and biogeochemistry. The main goal of this study is to evaluate the performance of the Los Alamos Sea Ice Model (CICE) to simulate physical and biogeochemical properties at time scales of a few weeks and to use the model to analyze ice algal bloom dynamics in different types of ice. Ocean and atmospheric forcing data and observations of the evolution of the sea ice properties collected from 18 April to 4 June 2015, during the Norwegian young sea ICE expedition, were used to test the CICE model. Our results show the following: (i) model performance is reasonable for sea ice thickness and bulk salinity; good for vertically resolved temperature, vertically averaged Chl *a* concentrations, and standing stocks; and poor for vertically resolved Chl *a* concentrations. (ii) Improving current knowledge about nutrient exchanges, ice algal recruitment, and motion is critical to improve sea ice biogeochemical modeling. (iii) Ice algae may bloom despite some degree of basal melting. (iv) Ice algal motility driven by gradients in limiting factors is a plausible mechanism to explain their vertical distribution. (v) Different ice algal bloom and net primary production (NPP) patterns were identified in the ice types studied, suggesting that ice algal maximal growth rates will increase, while sea ice vertically integrated NPP and biomass will decrease as a result of the predictable increase in the area covered by refrozen leads in the Arctic Ocean.

Plain Language Summary Important changes in the ice regime of the Arctic Ocean have occurred over the last decades with reductions in the summer sea ice extend and thickness. These changes and the importance of sea ice to the global climate system, the ecology of the Arctic Ocean, and the global biogeochemical cycles have justified the development of mathematical models to forecast sea ice evolution regarding its physical, chemical, and biological properties. In this work we test one such model—the Los Alamos Sea Ice Model—with data collected during the Norwegian young sea ICE expedition. Our results show that the model is capable of predicting accurately sea ice thickness, temperature, and salinity during a period of several weeks. However, it is not so accurate for biological variables. We suggest some aspects that may be investigated in trying to improve model performance, with emphasis on a better understanding of the behavior of ice algae that have an overwhelming importance for the Arctic marine food webs. Our results point to future changes in Arctic sea ice primary production associated with a more dynamic ice cover and a higher frequency of refrozen leads.

1. Introduction

Over the last decades, the sea ice regime of the Arctic Ocean has changed from a thick perennial multiyear ice (MYI) to predominantly thinner first-year ice (FYI) concomitant with a dramatic decline in summer sea ice extent [e.g., *Maslanik et al.*, 2011; *Barber et al.*, 2015]. The physical properties of FYI are different from those of MYI [*Hudson et al.*, 2013], suggesting that the changing ice regime may affect the feedbacks between sea ice, atmosphere, and ocean. Atmospheric changes seem to be the main driver of sea ice change, with positive feedbacks linked to reduced ice concentration, surface albedo, and ice thickness leading to

additional local atmospheric and oceanic influences and self-supporting feedbacks [*Döscher et al.*, 2014]. *Melnikov et al.* [2002] presented evidence of differences in the physical-chemical and biological characteristics of sea ice in the Arctic Ocean between the 1970s and late 1990s, including a major reduction in biodiversity of sea ice biota. The evolution of the icescape has and will continue to impact primary and secondary production and the geographical distribution of several species, as suggested by empirical and modeling studies [*Slagstad et al.*, 2011, 2015; *Jin et al.*, 2012, 2013; *Vancoppenolle et al.*, 2013a; *Ardyna et al.*, 2014; *Arrigo and van Dijken*, 2015]. Several studies have emphasized the role of sea ice in global biogeochemical cycles and fluid and gas exchanges with the sea and the atmosphere [e.g., *Vancoppenolle et al.*, 2013b]. Primary production has increased in the Arctic Ocean over the last years [*Jin et al.*, 2012; *Arrigo and van Dijken*, 2015]. However, future trends in primary production for the Arctic Ocean are less certain, depending on the interplay between an expected decrease in light limitation—following the reduction of sea ice extent and thickness—and trends in nutrient limitation—depending on changes in upper ocean stratification/mixing and inputs from land [*Popova et al.*, 2012; *Vancoppenolle et al.*, 2013a; *Slagstad et al.*, 2015].

The importance of physical properties of sea ice combined with a changing ice regime has stimulated the development of several mathematical models attempting to simulate sea ice dynamics and thermodynamics such as the Granular Sea Ice Model [*Sedlacek et al.*, 2007], the Louvain-la-Neuve Sea Ice Model [*Vancoppenolle et al.*, 2009], and the Los Alamos Sea Ice Model (CICE) [*Jeffery et al.*, 2011; *Hunke et al.*, 2015]. Models were also developed to simulate sea ice biogeochemistry, coupled with the cited physical models or as stand-alone applications. *Tedesco and Vichi* [2014] presented a synthesis of ice biogeochemical models published over the last 10 years (see Table 1 of the cited authors). These models can be classified in three groups, according to how the vertical distribution of ice algae and associated biogeochemical processes were represented [*Duarte et al.*, 2015]: (a) one-layer models of fixed thickness, (b) one-layer models of variable thickness, and (c) multilayer models.

Validation studies have been carried out to test some of the available sea ice models. Some of these studies focused on large spatial scales, attempting to test how accurately different models predicted sea ice concentration, distribution, and thickness in the Arctic Ocean or Southern Ocean [e.g., *Sedlacek et al.*, 2007; *Vancoppenolle et al.*, 2009; *Shu et al.*, 2015], whereas others tested models against observations at a local scale [e.g., *Arrigo et al.*, 1993; *Arrigo and Sullivan*, 1994; *Huwald et al.*, 2005; *Sedlacek et al.*, 2007; *Vancoppenolle et al.*, 2007; *Jeffery et al.*, 2011; *Pogson et al.*, 2011; *Turner et al.*, 2013; *Jeffery and Hunke*, 2014; *Wang et al.*, 2015], with a focus on different aspects of sea ice physics and biology.

Over the past 20 years thermodynamic and biogeochemical sea ice models have undergone a methodological evolution: (i) modeling sea ice as a pure solid phase, even though parameterizing the effects of brine on thermodynamic properties, to mushy layer dynamics (e.g., *Huwald et al.* [2005] versus *Turner et al.* [2013]); (ii) neglecting the effects of salinity on thermodynamics or prescribing a fixed salinity profile toward attempting to simulate salinity using different parameterizations (e.g., *Arrigo et al.* [1993] versus *Jeffery et al.* [2011]); and (iii) modeling biogeochemistry at the bottom ice toward vertically resolved biogeochemical models (e.g., *Jin et al.* [2008] versus *Pogson et al.* [2011]).

Synthesis of the modeling approaches employed so far also highlights the challenges in modeling sea ice thermodynamics, tracer dynamics, and biogeochemistry despite the achievements in recent years. We believe that these challenges are mainly related to processes that are more dependent on parameterizations, such as tracer dynamics and biogeochemical phenomena, where concepts are still poorly described [*Steiner et al.*, 2016], compromising model accuracy. Therefore, studies that provide insight into the strengths and weaknesses of available models are required. In spite of those challenges, models may be useful to test concepts and get insight into ongoing changes in the Arctic sea ice. Accordingly, the main goal of this study is to answer the following questions:

1. How accurately can we simulate sea ice physical and biogeochemical variables at time scales of a few weeks, in different types of ice?
2. Which are the most problematic prognostic variables and processes?
3. What are the main differences in ice algal bloom dynamics between different types of ice?

To address these questions we used forcing data obtained during the Norwegian young sea ICE (N-ICE2015) expedition carried out in the Arctic Ocean north of Svalbard from January to June 2015 [*Granskog et al.*, 2016].

The N-ICE2015 data sets include all necessary forcing time series to simulate sea ice thermodynamics and biogeochemistry of the ice floes monitored during the expedition at relevant temporal and spatial scales (floe scale).

2. Materials and Methods

During the N-ICE2015 expedition, RV *Lance* was used as a research platform to establish drifting ice camps in the southern Nansen Basin of the Arctic Ocean. The observational platform was designed to collect comprehensive data sets of the atmosphere-snow-ice-ocean-ecosystem interactions in a thinner Arctic sea ice regime. During the campaign, altogether four ice camps (Floes 1 to 4) were established that drifted with the ice pack [*Granskog et al.*, 2016]. This study uses data collected during the N-ICE2015 expedition, as described in detail in other papers [*Cohen et al.*, 2017; *Kauko et al.*, 2017; *Meyer et al.*, 2017a; *Olsen et al.*, 2017; *Peterson et al.*, 2017], to force simulations with version 5.1 of the Los Alamos Sea Ice Model (CICE) and to analyze the resulting output. The model applies mushy layer thermodynamics and vertically resolved biogeochemistry in a one dimensional (1-D) stand-alone mode [*Turner et al.*, 2013; *Hunke et al.*, 2015; *Jeffery et al.*, 2016].

2.1. Sea Ice Conditions and Study Period Used for Modeling

The origin and age of the oldest ice in the study region were examined by sea ice back trajectories based on the daily sea ice motion satellite product from ASCAT and SSS/I [*Girard-Ardhuin and Ezraty*, 2012]. The ice could be tracked back to the Laptev Sea in autumn 2013; thus, the oldest ice in the study area was second-year ice (SYI) [*Itkin et al.*, 2017]. Based on salinity and $\delta^{18}O$ profiles at the study site, the ice was found to be a mix of first-year (FYI) and second-year ice (SYI) with lower salinity in SYI [*Granskog et al.*, 2017]. Remnants of low salinity and $\delta^{18}O$ surface layers indicate that some ice survived one summer melt period, while other cores had typical FYI features [*Granskog et al.*, 2017]. Modal sea ice thickness in the area was 1.5 m for the FYI and SYI, and snow depth was 30 cm for the FYI and 50 cm for the SYI [*Rösel et al.*, 2016a; *Rösel et al.*, 2016b].

Model simulations of a refrozen lead (RL) and SYI sites were carried out in this study. For details of observations see *Kauko et al.* [2017] and *Olsen et al.* [2017]. These were part of a larger floe (Floe 3) that was monitored between 18 April and 5 June 2015 during the N-ICE2015 expedition, while the camp drifted from the Nansen Basin across and to the west of the Yermak Plateau (Figure 1). Simulations were carried out from 24 April, when the lead began refreezing, until 4 June.

2.2. Model Concepts and Approaches

Version 5.1 of CICE resolves physical processes vertically and biogeochemical processes in a single layer at the ice bottom and has been used in pan-Arctic biogeochemistry simulations coupled with ocean circulation models [*Jin et al.*, 2012]. It includes several interacting components to simulate ice transport, mechanical ridging, and thermohaline dynamics [*Hunke et al.*, 2015]. In addition, a 3-D sea ice biogeochemical module has been added to CICE [*Jeffery et al.*, 2016]. Only the thermohaline dynamics and the vertically resolved biogeochemistry components are active in 1-D simulations and are thus relevant to the present work.

The various components, algorithms, and software used in CICE are documented in technical manuals [*Hunke et al.*, 2015], and, more specifically, the biogeochemical processes, equations, and parameter values used in the present study are described in *Jeffery et al.* [2016]. Several papers have described and discussed in depth the modeling approaches followed in CICE: e.g., *Jeffery et al.* [2011] tested different ways of simulating the transport of tracers in sea ice; *Elliott et al.* [2012] presented results of a biogeochemical bottom layer model implemented in CICE; *Turner et al.* [2013] described a new parameterization of gravity brine drainage that is used in the present study; and a thorough sensitivity analysis of CICE v5.1 physical components was carried out by *Urrego-Blanco et al.* [2016].

Several upgrades were integrated in the code over time using more advanced approaches to simulate various sea ice components and processes. The configuration used in the present study includes mushy layer thermodynamics [*Feltham et al.*, 2006; *Hunke et al.*, 2015], a Delta-Eddington approach for albedo and shortwave radiation fluxes [*Hunke et al.*, 2015], the gravity drainage approach described in *Turner et al.* [2013], and the vertically resolved biogeochemical model described in *Jeffery et al.* [2016]. For the biogeochemical component, a generic ice algal group (diatoms) was selected. Its growth is limited by light, temperature, nitrogen

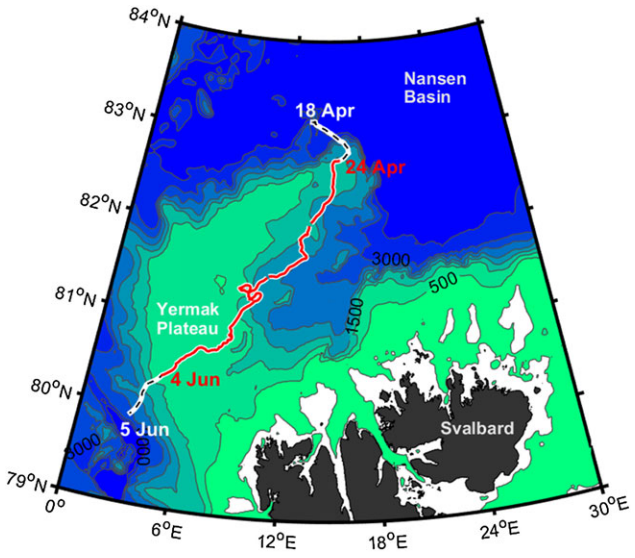

Figure 1. RV *Lance* drift between 18 April and 5 June 2015 during the drift of Floe 3 of the N-ICE2015 expedition, from the Nansen Basin and across the Yermak Plateau. The segment corresponding to the time span of the simulations described in this study is shown in red.

(ammonium and nitrate), and silicic acid using equations and parameters described in *Jeffery et al.* [2016]. Pennate diatoms were the dominant algal group in sea ice samples collected in the types of ice and periods simulated in this study [*Olsen et al.*, 2017].

In the case of 1-D stand-alone simulations, the sea ice model is forced by atmospheric and oceanographic time series that in the present study include the data sets listed below (see section 3). One of the forcing variables is the mixed-layer temperature (equivalent to sea surface temperature (SST) in the model), which is calculated via a thermodynamic slab-ocean mixed-layer parameterization within the CICE model, using a stability-dependent turbulent flux parameterization that is partially controlled by the mixed layer depth (MLD) parameter. Thus, SST and the salinity-dependent freezing temperature influence the exchange of heat between the ice and the ocean, based on the short wave radiation that reaches the sea through snow, ice, and open water; the heat exchanges between the water and the ice and atmosphere; and heat fluxes across the mixed layer. Water temperature is, however, also influenced by lateral and vertical mixing, not accounted for in the present model configuration. CICE includes a restoring time parameter that is used to assimilate measured water temperatures and bring values calculated by the slab-ocean mixed-layer parameterization close to observations, compensating for those processes not accounted for in the calculation of water temperature in the stand-alone configuration. In the present study, after testing several values, a restoring time scale of 1 day is used, similar to *Jeffery and Hunke* [2014]. An alternative could be forcing water temperature with observations and not attempting to modify it. However, this may not be a good solution since temperatures measured in the water are, by definition, above its freezing point, preventing the formation of frazil ice in the model. CICE calculates a freezing potential that allows the formation of frazil ice and is a function of the ocean-water energy budget. After some test runs, it became apparent that MLD, based on observed density gradients, may not be appropriate to reproduce ice thermodynamics, especially at short time scales, when the time required to modify the water temperature by the slab-ocean mixed-layer parameterization becomes too large and the formation of frazil ice in the RL simulation occurs almost 2 weeks later than in reality. We abbreviate the depth used in the simulations as hmix, implying a mixing depth range distinct from that of the MLD, as a way to parameterize vertical small-scale stratification and related thermodynamic processes. hmix was set to 15 m for all simulations. This mixing depth range reflected the typical range within which wind forcing penetrated and homogenized the surface layer during the N-ICE2015 expedition [*Meyer et al.*, 2017b]. The turbulent ocean heat flux measured at 1 m below the ice-ocean interface [*Peterson et al.*, 2016], which is used to force the simulations, is therefore assumed to be valid within this 15 m mixing-depth range. Ideally, the mixing-depth range would vary over time to better reflect observations, with larger values during storms and smaller values during quiet periods. However, the chosen mixing depth range provides reasonable results and is kept as a constant so as not to introduce additional complexity with respect to the interpretation of results.

Another forcing time series is that of current velocity relative to the ice. In its default configuration, the 1-D CICE setup uses a minimum default current velocity of 0.001 ms^{-1} to provide background-level shear between the water and the ice and thereby force heat exchanges. In the present study, we implemented calculation of shear in the 1-D mode from velocities measured at 1 m below the ice-ocean interface to better mimic realistic forcing. The shear calculation is done exactly in the same way as in the dynamical

component of CICE [*Hunke et al.*, 2015], thus allowing for results from this 1-D setup to be comparable with results from coupled CICE-ocean model simulations.

In CICE it may be assumed that diatoms may avoid ice melting to some extent due to the gliding capacity of some pennate species [*Aumack et al.*, 2014]. However, motility is not calculated as a function of environmental gradients. Motility may be an adaptation to optimize between vertically opposing factors, such as light and nutrients, as has been suggested for some microphytobenthic diatoms [*Saburova and Polikarpov*, 2003]. In the present study ice algal motility was implemented in CICE based on two different paradigms: (i) assuming that vertical motion is purely random but with a realistic velocity (default value used in CICE is 4.3 cm d^{-1}, within the velocity ranges reported in *Aumack et al.* [2014]), implying that ice algae may move up or down independent of any environmental gradients ("neutral model") and (ii) assuming that algae move toward the closest best conditions that minimize the impact of all limiting factors considered (light intensity, temperature, nitrate, and silicic acid concentrations), with the same velocity mentioned before ("deterministic model"). Therefore, if the minimum of all limiting factors is higher (closer to one) in a layer above or below the current layer, part of the algae migrates toward the "better" layer following an upwind scheme. The comparison between simulations with and without algal motion allows evaluating the possible effect of motility behavior, and the contrast between the "random" and the "deterministic" models allows testing the potential importance of vertical gradients in limiting environmental factors.

Equation (1) describes changes in ice algal concentration due to algal motion, and equation (2) is the numerical upwind version of (1).

$$\frac{dC}{dt} = \frac{d(v \bullet C)}{dx} \approx \frac{\Delta C}{\Delta t} = \frac{\Delta(v \bullet C)}{\Delta x} \tag{1}$$

$$\frac{\Delta C}{\Delta t} = \frac{\Delta(v \bullet C)}{\Delta x} \Leftrightarrow$$
$$\frac{C_i^{t+\Delta t} - C_i^t}{\Delta t} = \frac{0.5 \bullet \left[\left[(v + |v|) \bullet C_{i-1}^* + (v - |v|) \bullet C_i^*\right] - \left[(v + |v|) \bullet C_i^* + (v - |v|) \bullet C_{i+1}^*\right]\right]}{\Delta x} \tag{2}$$

where C is ice algal concentration (mM N m^{-3}), v is ice algal velocity (m s^{-1}) (positive downward following CICE sign convention for fluxes), x is vertical distance (m), i is layer index in the biological grid (biogrid is the grid that is used in CICE for biogeochemistry), and the asterisk is the time at which concentrations are reported (t in the case of using an explicit method and $t + \Delta t$ in the case of using an implicit method).

Model results for the periods described above (see section 2.1) are compared with observations of the following variables: sea ice thickness, temperature, salinity, nitrate, silicic acid, and chlorophyll (Chl *a*). CICE calculates biomasses in nitrogen units, and the conversion to Chl *a* (2.1 mg Chl *a* mmol N^{-1}) was chosen from the range reported by *Smith et al.* [1993]. The observed data show no significant correlation ($p > 0.05$) between particulate organic nitrogen (PON) and Chl *a*, not surprisingly, considering that the detritus and other nonalgal life forms also contribute to PON. However, the use of Chl *a* as a proxy for microalgal biomass is also questionable considering the high variance of the carbon:Chl *a* ratios. *Jørgensen et al.* [1991] report weight ratios in the range 22 to 288. This also implies a large variability of the nitrogen:Chl *a* ratio, making a proper comparison of the CICE output with Chl *a* data less reliable. The types and resolution of the data available from the RL and the SYI are not identical (Table 1), limiting the comparisons between model and observations. In some cases, data are vertically resolved, while in other cases, only vertically averaged data are available.

2.3. Model Simulations

The main purpose here it to disentangle the feedbacks between physical, chemical, and biological factors, in order to better understand some of the results observed during the N-ICE2015 expedition and also to pinpoint model shortcomings and possible improvements. Synergies between this study and several others included in this volume are frequently referred to.

It would be impractical to list here all the simulations that were carried out or even to present results for all the variables that were analyzed in each simulation. Thus, Table 1 synthesizes the main model simulations. The RL had more variables monitored with a higher temporal resolution than the other ice types. An ice mass balance buoy (IMB) [*Jackson et al.*, 2013] was used to monitor SYI providing snow and ice thickness and snow, sea ice, and surface seawater temperature with high temporal (6 h) and vertical resolutions (2 cm). Case

Table 1. Main Model Simulations[a]

Type of Ice	Variables Used for Model Evaluation	Simulations
Refrozen lead (RL)	Ice thickness, vertically averaged salinity, bottom nitrate and silicic acid concentrations, and vertically averaged ice algal Chl *a* concentration	RL_Sim_1: standard CICE parameter values; RL_Sim_2: diatom Si:N ratio reduced from 1.8 to 1.0 within ranges reported in *Brzrezinzki* [1985] (0.25–4.38) and *Hegseth* [1992] (0.50–1.30); RL_Sim_3: diatom half saturation constant for silicon uptake reduced in the same proportion as the Si:N from 4.0 to 2.2 μM within the range (1.1–4.6 μM) reported in *Nelson and Tréguer* [1992]. Other parameters as in the standard simulation; RL_Sim_4: algal recruitment increased in the same proportion as previous parameters. Other parameters as in the standard simulation; RL_Sim_5: decreased Si:N ratio and half saturation constant for silicon uptake as before and decreased recruitment in the same proportion
Second-year ice (SYI) with IMB data	Ice and snow thickness and vertically resolved ice temperature	SYI/IMB: standard CICE parameter values
Second-year ice (SYI) with coring data	Bottom nitrate and silicic acid concentrations and vertically resolved salinity and ice algal Chl *a* concentration	SYI_Sim_1: standard CICE parameter values, except for the sigma coefficient for snow grain (R_snow) [*Urrego-Blanco et al.*, 2016] that was changed from 1.5 to 0.8 (see section 4.4); SYI_Sim_2: "random" algal motion implemented; SYI_Sim_3: "deterministic" algal motion implemented; SYI_Sim_4: "deterministic" algal motion combined with lowered Si:N ratio and reducing the half saturation constant for silicon uptake as above

[a]The refrozen lead (RL) was monitored for more variables and with a higher temporal resolution than the remaining ice types. An area with SYI was monitored with minimal disturbance, using an ice mass balance (IMB) buoy (SIMBA-2015c) [*Jackson et al.*, 2013] that provided sea ice and surface seawater temperature data with high temporal (6 h) and vertical resolution (2 cm). Ice cores were collected at another location of the floe with SYI, and simulations were carried out for comparison with obtained biogeochemical data (refer to text).

simulations focus on comparing observed and simulated physical variables only. In another part of the ice floe—the main coring site—SYI was cored regularly and available biogeochemical data [*Kauko et al.*, 2017; *Olsen et al.*, 2017] are compared with simulations. Hereafter the main simulation sets will be identified as "RL," "SYI/IMB," or "SYI/coring."

Biogeochemical simulations were carried out changing ice algal recruitment, i.e., the flux of ice algae from the water to the ice, considering its very high uncertainty and importance for the RL simulations that started with no ice. Recruitment is based on the ice algal nitrogen concentration difference between the bottom ice and the ocean. A default value of 0.002 μM N is used for the ocean boundary in CICE [*Jeffery et al.*, 2016]. This value was increased/decreased in different simulations. Silicon-related limiting parameters—silicon:nitrogen (Si:N) ice algal ratio and the half saturation constant for uptake of silicic acid—were changed within ranges reported in the literature after strong evidence for silicon limitation, both from the empirical and the model data. The effects of algal motion were also investigated, using the approaches described in section 2.2.

A time step of 450 s was used in all simulations. Tests conducted with shorter time steps lead to similar results. Fifteen ice layers were used in all simulations and one snow layer for the RL or five for the SYI simulations. The RL simulations started with no ice, whereas SYI simulations were initiated with snow and ice conditions as similar as possible to the observed ones, after spinning up the model for some time to allow the production of ice. Initial ice contents for RL result from the incorporation of water properties during ice formation. Therefore, when frazil ice is formed, it has bulk properties similar to those of seawater at the same date. The model reads seawater salinity, temperature, and nutrient concentration (ammonium, nitrate, and silicic acid) values from the forcing function files. The SYI initial conditions were set to match observations of ice and snow thickness, salinity, nitrate, silicic acid, and ice algal biomass.

2.4. Evaluation of Model Performance

Several criteria synthesized in *Allen et al.* [2007] were used to evaluate the model results: (i) the Nash-Sutcliffe efficiency (ME) [*Nash and Sutcliffe*, 1970], which is a measure of the ratio of the model error to the variability of the data; (ii) the absolute value of the percentage of model bias |Pbias|—a measure of whether the model is

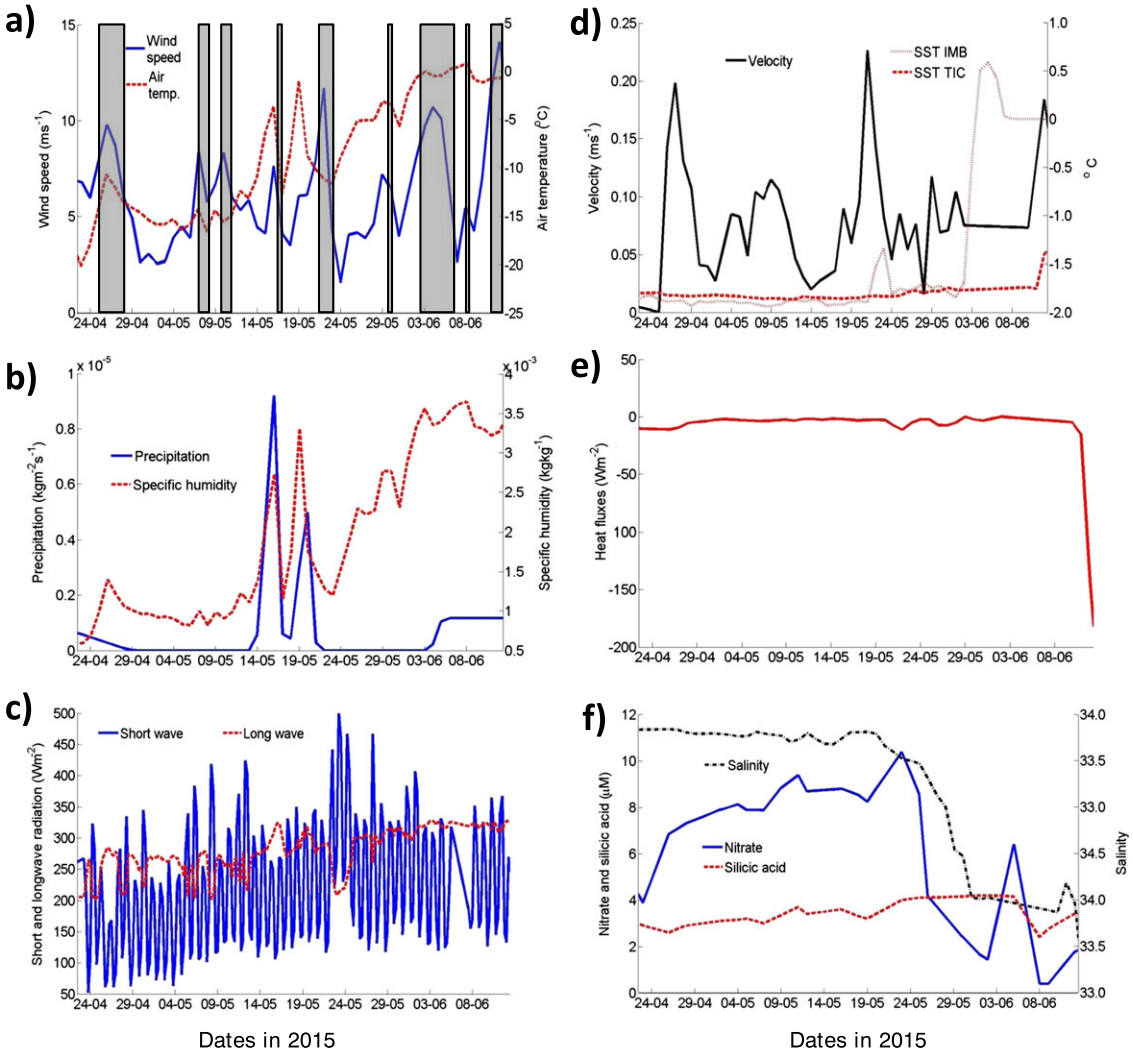

Figure 2. (a–f) Model forcing time series. (left and right) Atmospheric and ocean forcing, respectively. Air temperature is shown in °C in Figure 2a, but the input to the model is in °K. The graph also includes shaded areas indicating storm events [*Cohen et al.*, 2017]. Current velocity relative to the sea ice in Figure 2d, heat fluxes at 1 m below the ice-ocean interface in Figure 2e (negative heat fluxes are upward following CICE convention), and sea surface salinity data presented in Figure 2f were derived from a turbulence instrument cluster (TIC). Sea surface temperatures (SSTs) were also obtained from the TIC and from an ice mass balance buoy. Data are provided to the model with a daily frequency, except for incident short and longwave radiation data, which is used at 6 h frequency. The model interpolates forcing data to the defined time step (see section 3 data time series used for model forcing and evaluation).

systematically underestimating or overestimating the observations; (iii) the cost function (CF) that is a measure of the goodness of fit between different data sets [*Convention for the Protection of the Marine Environment of the North-East Atlantic (OSPAR) Commission*, 1998]; (iv) the root-mean-square error (RMSE); and (v) the squared correlation coefficient (r^2), which is a measure of the data variability explained by the model. Whenever available in the literature, qualitative criteria were adopted (Table S1 in the supporting information). Prior to apply any of the these measures of model reliability it was necessary to average empirical data for the same depth ranges as the model data and, in the case of vertically resolved data, it was necessary to interpolate both the empirical and the model data with the same spatial resolution to allow pairing of both data sets. When different measures of skill lead to controversial quality evaluations, the visual comparison of model and empirical data was also considered in judging model performance.

The variables selected for model evaluation with the above criteria were those for which there were more than five observations at different times coinciding spatially with the model results. These included the variables listed in Table 1, except vertically resolved salinity, nitrate, and silicic acid concentrations. Variables not fitting into the mentioned criteria were still visually compared with the best available data.

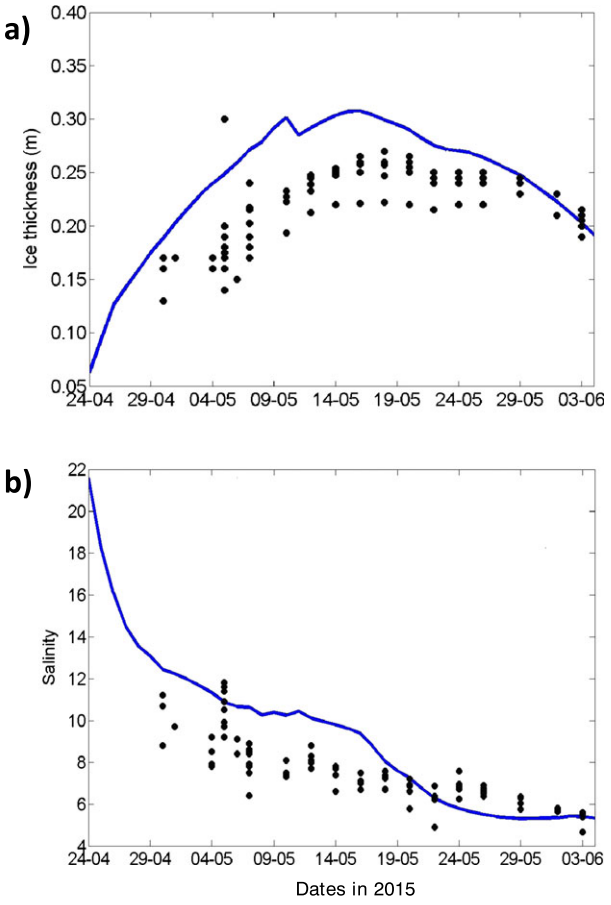

Figure 3. Results for the RL: observed (dots) and simulated (lines) (a) ice thickness and (b) vertically averaged bulk ice salinity (refer to text).

3. Data Time Series Used for Model Forcing and Evaluation

Several data sets were used to force and evaluate the model. Some of these are published and include the following: wind speed, air temperature, precipitation, and specific humidity [*Hudson et al.*, 2015; *Cohen et al.*, 2017]; incident surface short and longwave radiation data [*Taskjelle et al.*, 2016; *Hudson et al.*, 2016]; ice core physics—temperature and salinity sea ice data [*Gerland et al.*, 2017]; snow and ice thickness, ice temperature, and sea surface temperature (SST) from IMB data (SIMBA-2015c) [*Itkin et al.*, 2015]; sea surface current velocity, temperature, salinity, and heat fluxes from a turbulence instrument cluster (TIC) [*Peterson et al.*, 2016, 2017]; and sea surface nutrient concentrations [*Assmy et al.*, 2016].

RL simulations were forced with SST derived from the TIC data set, whereas SYI simulations were forced with SST from the IMB data set.

Moreover, other data sets on photosynthetically active radiation (PAR, 400–700 μm) transmitted through snow and ice, sea ice salinity, Chl *a*, nitrate and silicic acid, and snow thickness were also used. These have been described and discussed in other papers of this volume [*Gerland et al.*, 2017; *Taskjelle et al.*, 2017; *Kauko et al.*, 2017; *Olsen et al.*, 2017].

All forcing data sets and monitored sea ice data were obtained on, in, and below the same ice floe, within a radius of a few hundred meters. For the purposes of model forcing, data sets were interpolated linearly to fill in gaps and/or to properly synchronize with model data input routines.

4. Results

The forcing function time series are presented in section 4.1. Model results are described in sections 4.2–4.5. Due to space constraints, the results are not shown for all simulations. Unless otherwise stated, graphs that are not shown depict the same type of patterns across all simulations. Model results are daily averaged.

4.1. Forcing Functions

Forcing time series with daily frequency, except for radiation data that are presented with 6 h frequency, are shown in Figure 2. During the simulation period, there were nine storm events [*Cohen et al.*, 2017] indicated by the gray shaded areas in Figure 2a. Wind speed and air temperature ranged between 1.6 and 14.1 m s^{-1} and between −20.2 and +0.8°C, respectively (Figure 2a). Snow precipitation varied between 0 and 9.2×10^{-2} kg m^{-2} s^{-1}, and specific humidity varied between 6×10^{-4} and 4×10^{-3} kg^{-1} (Figure 2b). Incident short and longwave radiations were in the ranges 0–500 and 170–310 W m^{-2}, respectively (Figure 2c). Horizontal water velocity relative to the ice floe, measured at 1 m depth, varied from 0 to 0.22 m s^{-1} (Figure 2d). SST was between −1.9 and 0.6°C (Figure 2e). Daily heat fluxes at 1 m below the ice-ocean interface, measured with the TIC, ranged from slightly positive values to −180 W m^{-2} (Figure 2e).

Table 2. Model Performance for the Simulations Synthesized in Table 1 and for Selected State Variables According to the Nash Sutcliffe Model Efficiency (ME) [*Nash and Sutcliffe*, 1970], the Absolute Value of the Percentage Model Bias |Pbias|, the Cost Function (CF) [*OSPAR Commission*, 1998], the Root-Mean-Square Error (RMSE), and the r^2[a]

Simulations	Variables	ME	|Pbias|	CF	RMSE	r^2
RL_Sim_1	Ice thickness	Poor (−1.45)	Good (21.79)	Good (1.30)	0.05	0.45
	Vertically averaged salinity	Poor (−0.48)	Very good (19.78)	Good (1.00)	1.78	0.77
	Vertically averaged ice algal Chl *a* concentration	Poor (−0.32)	Poor (57.94)	Very good (0.85)	2.83	0.71
	Top ice algal Chl *a* concentration	Poor (−6.52)	Poor (90.28)	Reasonable (2.45)	1.50	0.85
	Bottom ice algal Chl *a* concentration	Poor (−1.52)	Poor (73.63)	Good (1.35)	6.97	0.77
	Chl *a* standing stock	Poor (−0.27)	Poor (55.4)	Very good (0.82)	0.64	0.58
RL_Sim_2	Vertically averaged ice algal Chl *a* concentration	Good (0.23)	Poor (42.26)	Very good (0.62)	2.17	0.72
	Top ice algal Chl *a* concentration	Poor (−5.51)	Poor (85.16)	Reasonable (2.31)	1.40	0.93
	Bottom ice algal Chl *a* concentration	Poor (−1.00)	Poor (66.06)	Good (1.21)	6.21	0.74
	Chl *a* standing stock	Good (0.27)	Poor (42.08)	Very good (0.63)	0.48	0.56
RL_Sim_3	Vertically averaged ice algal Chl *a* concentration	Good (0.47)	Good (38.70)	Very good (0.57)	1.79	0.66
	Top ice algal Chl *a* concentration	Poor (−6.36)	Poor (88.78)	Reasonable (2.41)	1.49	0.64
	Bottom ice algal Chl *a* concentration	Poor (0.05)	Poor (45.81)	Very good (0.84)	4.26	0.81
	Chl *a* standing stock	Good (0.42)	Poor (42.54)	Very good (0.63)	0.43	0.46
RL_Sim_4	Vertically averaged ice algal Chl *a* concentration	Poor (0.01)	Poor (48.88)	Very good (0.72)	2.46	0.69
	Top ice algal Chl *a* concentration	Poor (−6.35)	Poor (88.81)	Reasonable (2.41)	1.48	0.71
	Bottom ice algal Chl *a* concentration	Poor (−0.90)	Poor (63.74)	Good (1.17)	6.06	0.79
	Chl *a* standing stock	Poor (0.04)	Poor (48.60)	Very good (0.72)	0.55	0.52
RL_Sim_5	Vertically averaged ice algal Chl *a* concentration	Excellent (0.66)	Good (35.22)	Very good (0.52)	1.43	0.67
	Top ice algal Chl *a* concentration	Poor (−5.42)	Poor (84.45)	Reasonable (2.30)	1.39	0.89
	Bottom ice algal Chl *a* concentration	Poor (0.18)	Poor (40.14)	Very good (0.74)	3.98	0.81
	Chl *a* standing stock	Very good (0.54)	Good (37.71)	Very good (0.56)	0.38	0.55
SYI/IMB	Vertically resolved temperature	Excellent (0.81)	Excellent (9.89)	Very good (0.36)	0.47	0.96
SYI_Sim_1	Chl *a* standing stock	Good (0.36)	Good (25.05)	Very good (0.62)	0.56	0.86
	Vertically resolved ice algal Chl *a* concentration	Poor (−0.27)	Poor (56.75)	Very good (0.73)	1.15	0.00
SYI_Sim_2	Chl *a* standing stock	Good (0.40)	Good (24.40)	Very good (0.61)	0.54	0.85
	Vertically resolved ice algal Chl *a* concentration	Poor (−0.01)	Poor (50.29)	Very good (0.65)	1.02	0.02
SYI_Sim_3	Chl *a* standing stock	Good (0.38)	Good (25.00)	Very good (0.62)	0.55	0.69
	Vertically resolved ice algal Chl *a* concentration	Poor (−1.22)	Poor (77.67)	Good (1.00)	1.52	0.00
SYI_Sim_4	Chl *a* standing stock	Excellent (0.78)	Very good (14.73)	Very good (0.37)	0.32	0.94
	Vertically resolved ice algal Chl *a* concentration	Poor (−0.31)	Poor (59.98)	Very good (0.78)	1.17	0.02

[a]Quality levels for the first three parameters are based on data presented in Table S1 following *Maréchal* [2004] and *Radach and Moll* [2006]. Variables were selected for the evaluation of model performance depending on data availability and quality (see section 2.4). Regarding the refrozen lead simulations (RL Sim 1–RL Sim 5), model performance for the variables *ice thickness* and *vertically averaged salinity* is presented only for RL Sim 1 because model results are similar to the other four simulations. All values are dimensionless except the RMSE that is given in the same units of the variables shown in the second column—m for ice thickness, mg m^{-3} for Chl *a* concentration, and mg m^{-2} for Chl *a* standing stocks. "Top" and "bottom" Chl *a* concentrations refer to values that were averaged for the bottom 10 cm and for the remaining of the ice column, respectively.

Here the negative sign indicates an upward flux, following CICE convention. Salinity varied between 33.6 and 34.3, at the surface, whereas nitrate and silicic acid varied between 0.4 and 10.4 μM and between 2.4 and 4.2 μM, respectively (Figure 2f).

4.2. Refrozen Lead

Measured ice thicknesses of RL reached 0.27 m [*Kauko et al.*, 2017]. Measurements began approximately a week after ice started to build up in the lead that opened next to RV *Lance*. Simulated ice thickness ranged from zero, on the date corresponding to the opening of the lead (24 April), and a maximum in excess of 0.3 m, with a positive bias of up to 0.05 m (Figure 3). Minimum ice buildup is forecasted when assuming hmix variable and equal to the MLD (not shown), with frazil ice forming only on 9 May. Using hmix values $<$15 m leads to overestimation of ice melting toward the end of the simulation (not shown). Model performance is poor regarding ME and good for both |Pbias| and CF. RMSE was 0.05 m, and r^2 implies that the model explains 45% of the data variability (Table 2).

Measured bulk salinities varied between 4.6 and 11.8. Observed and simulated salinities show a decreasing trend over the study period. Model performance is poor regarding ME, very good for |Pbias|, and good for CF. RMSE is 1.78 and r^2 0.77 (Table 2). Shortwave transmittance simulated by the model is in accordance with measured values and around 0.2 [*Kauko et al.*, 2017] (not shown).

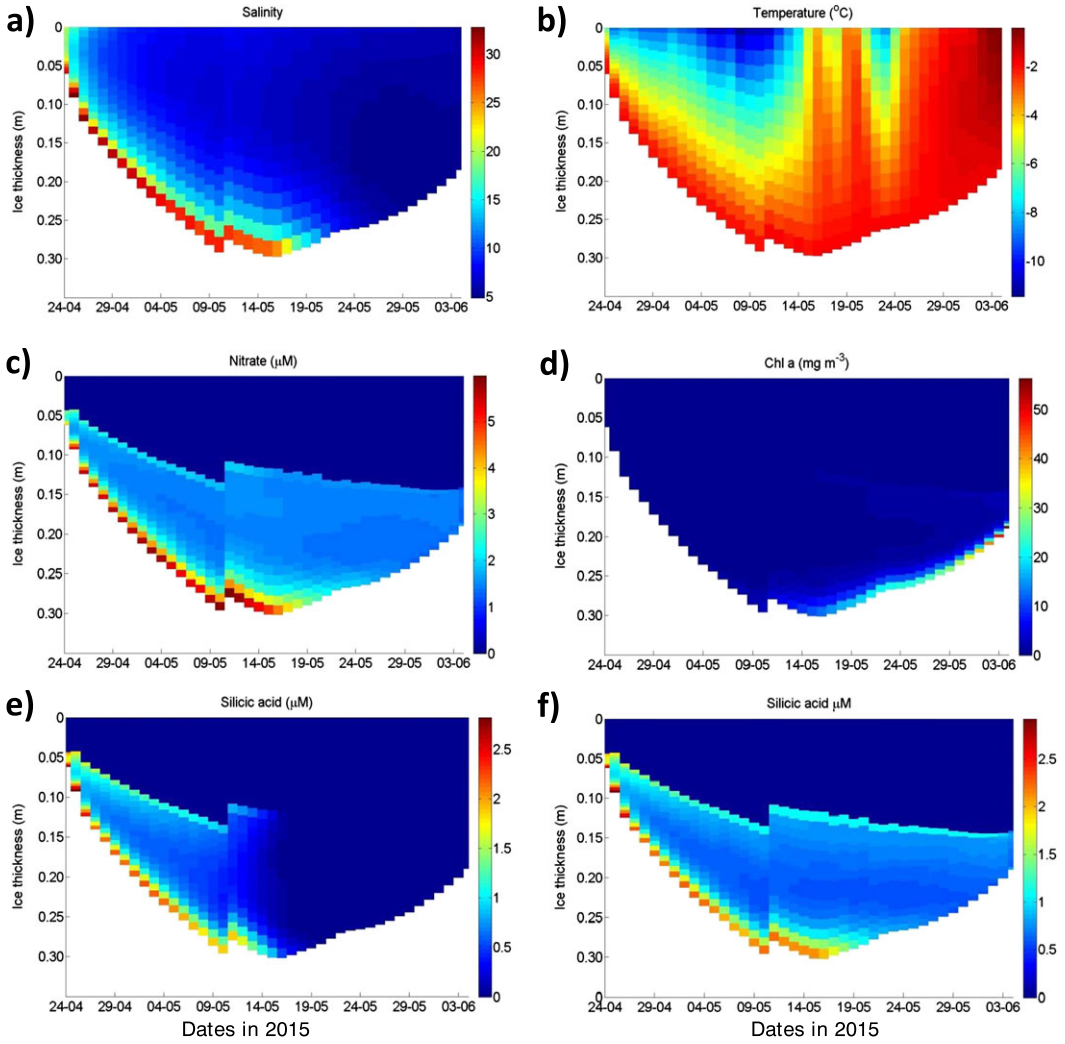

Figure 4. Results for the RL: simulated evolution of (a) ice salinity; (b) temperature; (c) nitrate; (d) ice algae Chl *a*; (e) silicic acid from RL_Sim_1 (Table 1); and (f) silicic acid in a simulation without biological uptake (not shown in Table 1), as a function of time and depth in the ice (refer to text).

Vertically resolved model outputs for sea ice bulk salinity show a sharp increase toward the bottom, with salinities up to 32.6, a slight increase near the top and with an almost uniform profile by the end. Minimum values (~5) are roughly midway between top and bottom ice (Figure 4a). During the period of ice melt, bottom salinity decreases to <10. Simulated sea ice temperature is between −11.5 and −0.4°C. Temperature increases from the ice top toward the bottom until 14 May when the air temperature became higher. Subsequently, there are two sea ice warming events that are in parallel with peaks in air temperature (Figures 2a and 4b). During these periods vertical temperature gradients fade away. After 24 May, the temperature gradient becomes opposite to that observed during the period of ice growth (between 24 April and 14 May), with surface values close to 0°C following the increase in air temperature (Figure 2a). Modeled nitrate concentrations are maximal at bottom ice with values of up to 5.8 μM and correlate with the evolution of measured sea-water values during the period of ice growth (Figures 2f and 4c). The model simulates an increase in ice algae at the ice bottom after the onset of melting toward the end of the simulation period, with concentrations in excess of 50.0 mg Chl *a* m^{-3}. Model-calculated silicic acid concentrations are strongly reduced by biogeochemical activity as seen when contrasting two simulations with and without biogeochemical uptake of silicic acid, respectively (Figures 4e and 4f). A similar comparison for nitrate shows no significant differences (not shown). The color patterns of Figures 4c and 4f show the time-dependent vertical extent of the biological grid (biogrid) of CICE. Vertical transport equations for biogeochemical

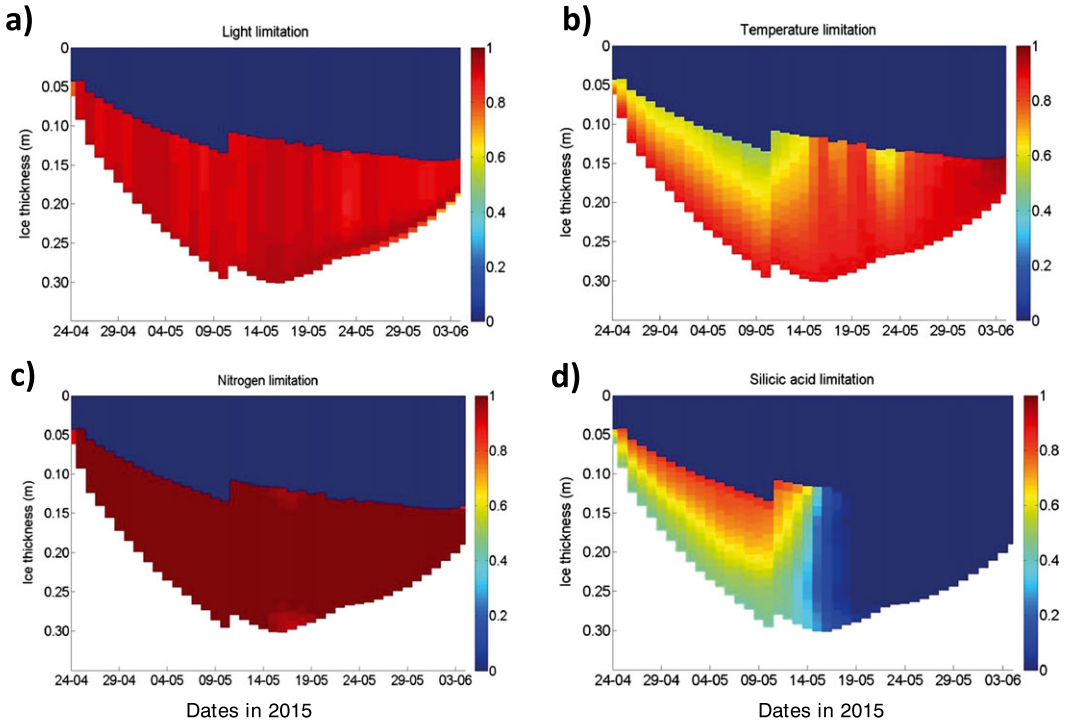

Figure 5. Results for the RL: simulated evolution of limiting factor values for (a) light; (b) temperature; (c) nitrogen; and (d) silicic acid from RL_Sim_1 (Table 1), as a function of time and depth in the ice. The upper regions of the graphs with zero values for all limiting factors correspond to the levels that are above the CICE biogrid and where there is no brine network (refer to text).

tracers are defined only where brine is present [*Jeffery et al.*, 2016]. The brine network extends roughly from 0.05 m from the ice top, at the beginning of the simulation, and almost from 0.15 m, toward the end, until the ice bottom. Brine nutrient concentrations (including ammonium) are shown in Figure S1 in the supporting information with values ranging from near 0 to 1 order of magnitude higher than maximal bulk values (Figure 4).

Limiting factor values for light intensity, temperature, nitrogen (ammonium + nitrate), and silicic acid concentrations in the brine (Figure 5), in the RL standard simulation (Table 1), vary between zero (maximum limitation) and one (no limitation), with lowest values/higher limitation for silicic acid, especially after 14 April, when ice algae concentration begins to increase. The upper regions of the graphs with zero values for all limiting factors correspond to the ice levels that are above the CICE biogrid and where there is no brine network.

The model underestimates bulk nitrate concentrations at the bottom 10 cm (Figure 6a). Empirical data show an increase in the averaged chlorophyll concentrations for the whole ice core and for the bottom 10 cm, until the end of the simulated period (Figures 6b and 6c). Model data, irrespective of the simulation, show also an increasing trend for the former but not for the latter. The standard simulation (RL_Sim_1) underestimates the observations. This underestimation is decreased by reducing the Si:N ratio (RL_Sim_2) from 1.8 to 1.0 or the silicon half saturation constant from 4.0 to 2.2 μM (RL_Sim_3) or increasing recruitment in the same proportion (refer to Table 1). Recruitment and the half saturation constant are the least and the most influential in the model output. Combining a reduction in recruitment with a decrease in both the Si:N ratio and the silicon half saturation constant in the same proportions as before holds a better fit between model and observations (RL_Sim_5). The improvement in the model goodness of fit and the reduction in the model bias as a function of some of the described parameter changes are reflected in the ME, CF, and |Pbias| values for vertically averaged Chl *a* concentrations, with emphasis on the results of RL_Sim_5 (Table 2), where all quality criteria are between good and excellent. Model skill for Chl *a* concentrations at (Figure 6c) or above (not shown) the bottom 10 cm is lower than that for vertically averaged Chl *a*. Chl *a*

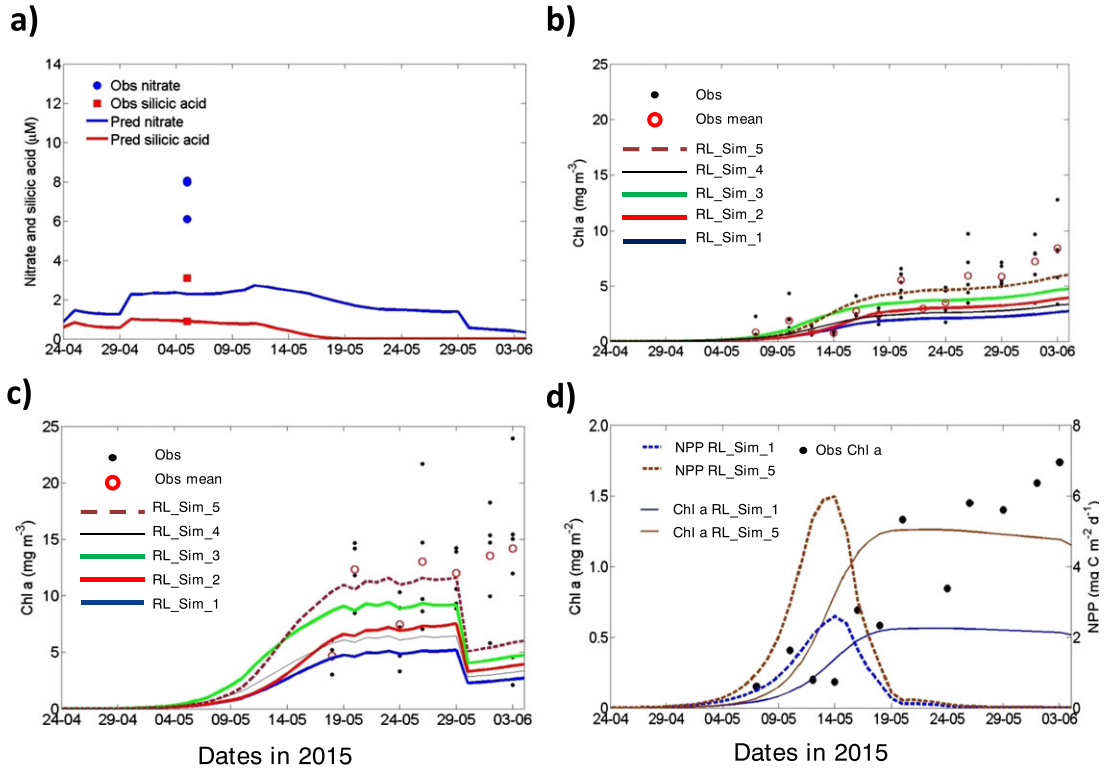

Figure 6. Results for the RL: (a) observed and simulated (RL_Sim_1) nitrate and silicic acid concentrations at the bottom 10 cm of the sea ice; (b) observed and simulated depth-averaged Chl *a* concentration for the whole ice column (all simulations); (c) observed and simulated Chl *a* concentration values averaged for the ice bottom 10 cm and for all simulations; (d) observed and simulated Chl *a* standing stocks (vertically integrated concentrations for the whole ice column) and simulated net primary production (NPP) for simulations RL_Sim_1 and RL_Sim_5 (refer to Table 1).

standing stocks (vertically integrated Chl *a* concentrations) and net primary production (NPP) are shown only for RL_Sim_1 and RL_Sim_5 (Figure 6d). In both cases the standing stock increases steeply, followed by a plateau, with a slightly negative trend. Observed standing stocks have a very large scatter but are comparable with RL_Sim_5 results. Sharp and narrow NPP peaks match the increase of the standing stocks. Model skill patterns for Chl *a* standing stocks are expectably comparable to those for vertically averaged Chl *a* (Table 2). However, the former are also influenced by any bias in simulated brine volume vertical distribution.

4.3. Second-Year Ice/Ice Mass Balance Buoy

IMB data for SYI show a depth-gradient trend in the sea ice temperature profile, with values increasing from the low atmospheric temperatures to warmer ocean levels. This gradient decreases during the measurement period (Figure 7a), and the ice becomes nearly isothermal at the end of the time series. Similar trends are reproduced by the model (Figure 7b). The observations and the model also show a gradual warming from the atmosphere connected to the positive air temperatures toward the end of the time series. Model performance for vertically resolved sea ice temperature is the best of all shown in Table 2 and is between very good for the CF and excellent for ME and |Pbias|.

4.4. Second-Year Ice/Main Coring Site

The model baseline simulation underestimates irradiance below the sea ice. Changing the default value of the sigma coefficient for snow grain (R_snow)—a delta-Eddington parameter that gives the standard deviation of the snow grain size [*Urrego-Blanco et al.*, 2016]—has a strong effect on simulated light intensity. The best fit was obtained with R_snow = 0.8 (Figure 8a). Therefore, this value was used in the SYI simulations. For most of the simulation period, ice-transmitted PAR was <2 μmol photons m^{-2} s^{-1} [*Taskjelle et al.*, 2016]. The model calculates a considerable increase in under-ice PAR toward the end of the simulation when melting occurred.

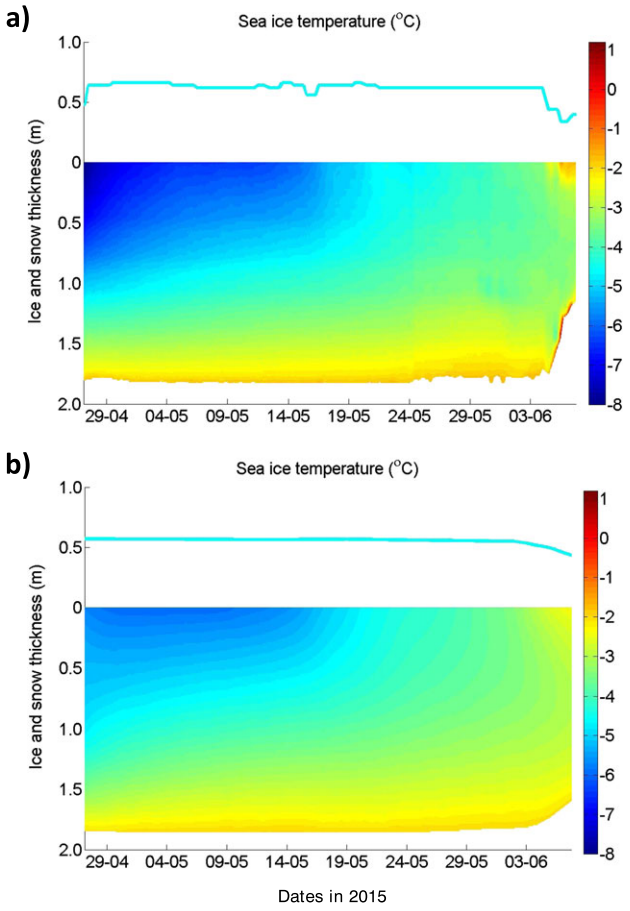

Figure 7. Results for the SYI/IMB: (a) observed and (b) simulated sea ice and snow thickness and sea ice temperature. Observed values are from a SIMBA ice mass balance buoy. The blue line above each plot shows snow height (refer to text and Table 1).

Salinity measurements show a large scatter, making it difficult to properly assess model performance. In spite of that, model results are within the range of observations before the onset of melting. Also, the simulated vertical gradients are similar to those observed (Figure 8b). Modeled and observed silicic acid at the bottom 10 cm of SYI exhibit very low values <1.0 μM that are very close to the detection limit of the method used for silicic acid quantification (0.7 μM) [*Grasshoff*, 1965], reason why measures of model skill were not applied here. For nitrate, model results are within the range of the few observations available (Figure 8c).

Chl *a* standing stocks and net primary production (NPP) are shown for SYI_Sim_1, 3, and 4 (Figure 8d). In all cases the standing stock increases, followed by a plateau, with a slightly positive trend in SYI_Sim_4, before a final decline. Simulated standing stocks underestimate observations toward the end of the simulated period with the exception of SYI_Sim_4, which shows a later and higher NPP maximum. NPP peaks match the increase of the standing stocks. More or less, recruitment has no effects on the model outputs because SYI contains Chl *a* in excess relative to that assumed for the ocean. Model performance for Chl *a* standing stocks is between good for ME and |Pbias|, very good for the CF for all simulations but SYI_Sim_4, where it is excellent for ME, and very good for the other two parameters (Table 2).

Vertically resolved model outputs for sea ice salinity show a relatively stable profile along the simulation period, except for the bottom layers where variability is larger. Salinity increases toward the bottom ice to values of 15 (Figure 9a). Temporal and vertical variabilities and ranges in sea ice temperature (Figure 9b) are very similar to what was described before for the SYI/IMB. Nitrate bulk concentrations (Figure 9c) are higher at the bottom ice and decrease to values <2 μM toward the end of the simulation period, at the onset of ice melting. Silicic acid shows the most noticeable decrease over the simulation period (Figure 9d), especially at intermediate layers where it decreases from 0.6–0.7 μM to nearly zero values. Maximum values (close to 0.8 μM) are observed at the bottom layer and the two layers closest to the ice top. A comparison between results obtained with and without biological uptake shows no significant differences in simulated nitrate concentrations but much larger silicic acid values in the former simulation (Figure S2). Observed Chl *a* ranged between <0.1 and 9.0 mg m^{-3}. Maximum values were observed at ice bottom or within 0.2 m from the bottom (Figure 9e). On several occasions more than one peak of Chl *a* was observed. The model (SYI_Sim_1) calculates a slight increase in Chl *a* values in the ice interior (approximately from 0.4 to 1.0 m from the ice upper surface) (Figure 9f). The simulated patterns are not similar to those observed. Implementation of random algal motion (SYI_Sim_2; Table 1) results in a considerable vertical displacement of the initial Chl *a* (Figure 9g). Using deterministic algal motion (SYI_Sim_3; Table 1) two maxima emerge at top and bottom ice (Figure 9h). Tests conducted with other model setups combined with deterministic algal motion also led to

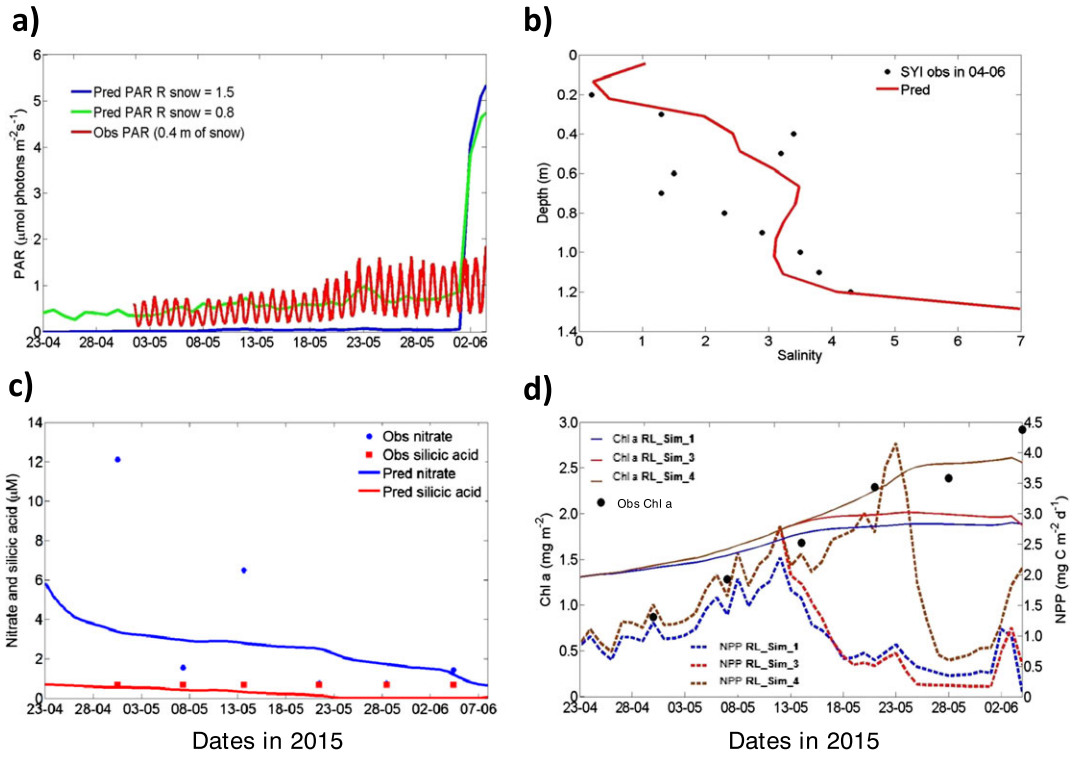

Figure 8. Results for the SYI/coring: (a) observed (red line, 15 s interval) and simulated daily averaged (SYI_Sim_1) photosynthetically active radiation (PAR) under the ice. Observed data were obtained with a TriOS Ramses sensor under ~1.4 m of ice and ~0.4 m of snow, between 26 April and 4 June, but values before 1 May were close to zero or below the instrument sensitivity [*Taskjelle et al.*, 2016]. Model data were obtained using 1.5 and 0.8 for the parameter R_snow. (b) Observed and simulated (SYI_Sim_1) salinities as a function of depth in the ice on 4 June. (c) Observed and simulated (SYI_Sim_1) nitrate and silicic acid concentrations at the bottom 10 cm. (d) Observed and simulated Chl *a* standing stocks and simulated net primary production (NPP) for simulations SYI_Sim_1, SYI_Sim_3, and SYI_Sim_4. Refer to Table 1 for a description of model simulations.

more than one maximum, including one at the bottom ice. Model performance for vertically resolved Chl *a* concentration is poor for ME and |Pbias| and for all simulations. The results obtained with CF are between good and very good (Table 2).

The brine network extends roughly from ~0.05 to 0.1 m from the ice top until the ice bottom. Brine nutrient concentrations (including ammonium) are shown in Figure S3. Very high values are obtained for nitrate and silicic acid in the upper parts of the brine network, during an initial period of some ice growth, when air temperature remained <-10°C (Figure 2a), with concentrations 3–4 orders of magnitude higher than maximal bulk values (Figures 9c and 9d).

Limiting factor values for light intensity, temperature, nitrogen (ammonia + nitrate), and silicic acid concentrations in the brine (Figure 10) show lowest values for silicic acid, especially after 13 April, and for light intensity before the onset of snow and ice melt.

4.5. Energy Budgets

Sea ice energy budgets computed from CICE results for the RL and for both SYI simulations are shown in Figure S4. In all cases, longwave fluxes are dominant, while down and upward fluxes practically cancel each other out. The amount of shortwave radiation absorbed by the RL is higher than that absorbed by the thick ice due to the thick snow cover on the latter. In the RL case, there is a positive correlation with a time lag between latent heat exchanges, the net energy budget, and the ice/snow-atmosphere sensible heat fluxes. In the SYI cases, the magnitude of these fluxes is much smaller, except after the onset of melting, when ice-ocean heat flux drives a large net positive flux.

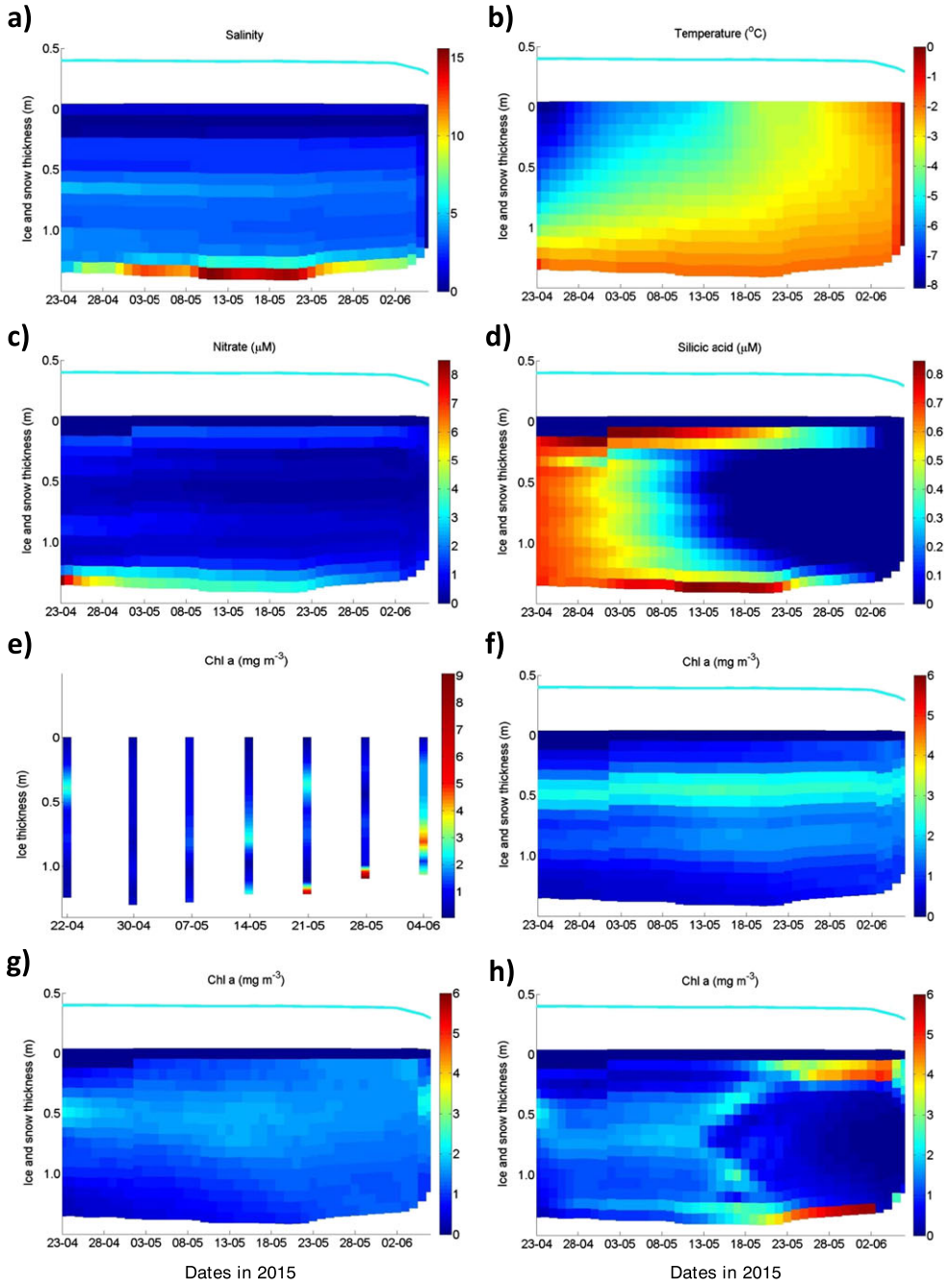

Figure 9. Results for the SYI/coring: simulated (a) bulk ice salinity; (b) temperature; (c) nitrate; (d) silicic acid; (e) observed Chl *a*; simulated (f) Chl *a* in SYI_Sim_1; (g) Chl *a* in SYI_Sim_2; and (h) Chl *a* in SYI_Sim_3. The blue line represents snow height (refer to Table 1). Note the differences in the color range between Figure 9e, on one hand, and Figures 9f, 9g, and 9h, on the other hand.

5. Discussion

5.1. Model Forcing and the Importance of Storms

Model forcing time series showed large increases in wind speed and air temperature during or close to storm events (Figure 2a). The same applied to current velocities and ocean heat exchanges (Figures 2d and 2e). The importance of these events on the variability of atmospheric and oceanographic conditions has been discussed in *Cohen et al.* [2017], *Meyer et al.* [2017a, 2017b], and *Peterson et al.* [2017]. Storms transport heat

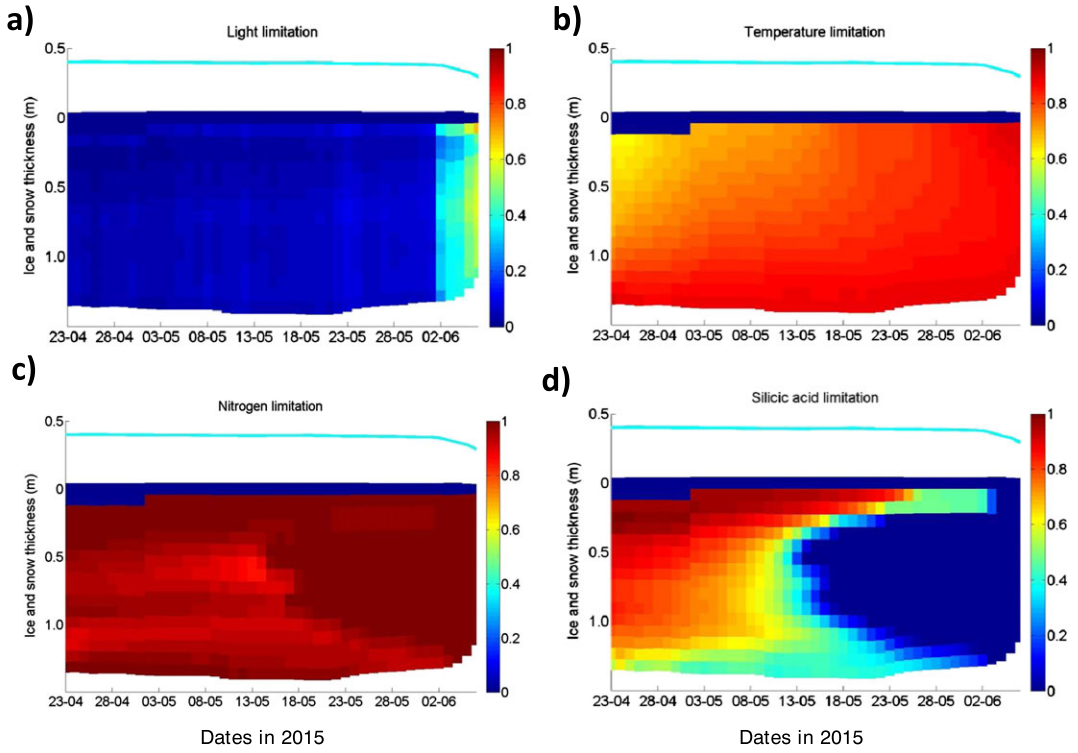

Figure 10. Results for the SYI/coring: simulated evolution of limiting factor values for (a) light, (b) temperature, (c) nitrogen, and (d) silicic acid as a function of time and depth in the ice in SYI_Simulation_1. The blue line represents snow height. The upper layers of the graphs with zero values for all limiting factors correspond to the levels that are above the CICE biogrid and where there is no brine network (refer to text).

and moisture from lower latitudes, and the strong winds associated with them drive sea ice drift and upper ocean mixing, increasing the heat flux from the ocean by an order of magnitude with potential consequences for sea ice melting. Storms also cause sea ice divergence and the opening of leads such as the RL discussed here [*Itkin et al.*, 2017].

Model results for the RL case, representative of new ice growth, showed the effects of storm events on sea ice thermodynamics in the form of two temperature peaks around May 19–20 (Figure 4b). This rapid ice warming is partly explained by low insulation due to the simulated snow accumulation (not shown) of just a few millimeters, due to the low snow precipitation during the simulation period. The observed accumulation reached maximal values of 0.02–0.06 m [*Kauko et al.*, 2017] but was very heterogeneous, presumably due to snow redistribution by wind. *Jeffery and Hunke* [2014] discussed the sensitivity of the ice physical state to snow cover and ran simulations with a prescribed snow fall to reproduce the observed snow cover and avoid the model bias caused by an inaccurate snow forecast. The insulating effect of snow explains the lack of warming "peaks" in the case of the SYI/IMB observations and model results (Figure 7). Here warming is strongly related to an increase in the ice-ocean heat exchanges as RV *Lance* drifted across the Yermak Plateau encountering warm Atlantic Water closer to the surface [*Meyer et al.*, 2017a; *Peterson et al.*, 2017]. The same applies to the SYI/coring case. In both SYI simulations, there is a small snow depth variability explained by the low snow fall rates. Observed variability was larger and likely related to wind redistribution, which is not taken into account in CICE.

The relatively high air temperature, precipitation, and specific humidity associated with the storm event that took place between 14 and 19 May (Figure 2a) contributed to reduced latent heat losses from the RL in two occasions during the mentioned period (see the two peaks of the red line in Figure S4a), leading to an increase in the net energy budget from negative to slightly positive, ice warming (Figure 4b) and an increase in sensible heat losses to the atmosphere. Therefore, one of the fluxes of smaller magnitude may have a determinant effect in shifting the net energy budget from negative to positive. The magnitude of the

ice-ocean heat exchanges increased both in the RL and the SYI simulations at the end of June. Also, slightly positive air temperatures explain some snow melting that leads to an increase in absorbed shortwave radiation in the SYI cases. The downward migration of the brine channel network in the RL resulted first from the low temperatures at the ice top and, at a later stage, from refreezing of melted snow ice. RL warming events in mid-May were driven by atmospheric forcing, while those at the beginning of June were ocean driven. The former are not apparent in the SYI simulations due to snow insulation. The impact of these sudden warming events on biogeochemical processes is not yet well understood. However, by changing ice temperature, they may have implications on ice salinity, density, and on the brine channel network, thereby influencing the exchange of nutrients and the organisms depending on them.

5.2. Sea Ice Thickness and Salinity

The results presented in Table 2 concerning model performance suggest that the CF is too optimistic in classifying all model results between reasonable and very good. Ice thickness seemed adequately reproduced for both the RL and the SYI/IMB cases (Figures 3a and 7). However, ME values show that model error is relatively large when compared with data variability (Table 2). On the other hand, model bias is relatively low and the RMSE is small (5 cm). Considering this somewhat controversial evidence from the various measures of model skill and the graphical model output, one is tempted to classify model results as, at least, reasonable.

Model-calculated ice thickness, heat exchanges, and melt rates are quite sensitive to surface current velocity, which is used to compute the heat transfer coefficient in the CICE model [*Hunke et al.*, 2015]. Simulations performed without the effects of current velocity underestimated ice melting (not shown). The timing of frazil-ice formation and initiation of ice growth in the RL case was quite sensitive to the depth of hmix (not shown) due to the time required to cool down the water to the freezing temperature. Depending on the vertical resolution of circulation models coupled with CICE, some positive bias may be anticipated in the time required for freezing open leads if the surface model layer is very thick. These small-scale processes may be quite important not only for simulations of the energy budget of the Arctic Ocean but also for biogeochemical processes. Indeed, refrozen leads that are covered with thin ice and a thin snow layer have a different thermodynamic behavior than thick ice with thick snow cover, as shown in Figure S4. They also act as "windows" allowing greater penetration of shortwave radiation into the water column compared to the thicker snow-covered ice [*Kauko et al.*, 2017], with local enhancement of phytoplankton primary production in the water column [*Assmy et al.*, 2017]. Observations and sampling conducted by divers under the RL identified assemblages of ice algae covering submerged ice blocks and some vertical ice walls at pressure ridges that had formed at the transition zone between the RL and the thicker ice. Also, empirical data show that Chl *a* concentration grew rapidly in thin ice from early May to the beginning of June (Figure 6b) [*Kauko et al.*, 2017], and estimated growth rates were up to 0.27 divisions per day [*Olsen et al.*, 2017].

The representation of the early evolution of the sea ice salinity profile will become more important in models, as the seasonal sea ice fraction of the Arctic ice pack increases [*Turner et al.*, 2013]. Laboratory and field experiments have been carried out regarding the initial stages of ice formation, including measures of (i) salt and brine fluxes at the bottom ice/water interface from brine expulsion during sea ice growth [*Wakatsuchi and Ono*, 1983]; (ii) vertical profiles of brine volume, salinity, and temperature [*Cottier et al.*, 1999]; and (iii) temperature, porosity, brine and bulk salinities, and liquid fraction [*Notz*, 2005; *Notz and Worster*, 2008]. The results of the former two studies were used by *Jeffery et al.* [2011] to validate a vertical transport model for sea ice tracers implemented in CICE. The results of Notz and coworkers were used by *Turner et al.* [2013] to test a 1-D parameterization of gravity drainage, based on mushy layer theory and also implemented in CICE and used in the present study. The results presented in Figure 3 suggest a good fit between simulated and observed vertically averaged bulk salinities for new ice (RL). The model shows a small positive bias. However, this bias may not be real because salinity measurements were taken from melted core samples, and during coring and the sampling procedure, some brine may be lost, leading to an underestimation of measured salinity. As with ice thickness, model error is relatively large when compared with data variability (Table 2), whereas model bias is low and the RMSE is small (1.78). Model results show an initial rapid drop in salinity followed by a slower decrease after 29 April 2015. These two different rates are a result of the two desalinization modes described in *Turner et al.* [2013]. After 14 May, there is another increase in desalinization related to melting. The lack of vertically resolved salinity data for the RL prevents a comparison

between vertical profiles. Such a comparison was done for SYI (Figure 8b), but it is not conclusive given the scatter of some data points.

5.3. Sea Ice Biogeochemistry

RL simulations showed a negative bias in bottom nutrient concentrations with nitrate lower than observed on 5 May (Figure 6a). However, the relatively high observed values are counter intuitive because the same brine exchanges responsible for desalinization (Figure 3b) force nutrient exchanges between the seawater and the ice. These exchanges cannot lead to bulk ice concentrations as high as seawater concentrations since only the brine volume is exchanged. Therefore, nutrient concentrations should scale with salinity in the absence of biological consumption. In the presence of ice algal growth, nutrient concentrations should be even lower, unless recycling could compensate for consumption. However, it seems rather unlikely that recycling could raise bulk concentrations above sea-water values, unless there was a large reserve of organic matter in the ice—very unlikely in newly formed ice. Another way to conciliate observed ice bulk nitrate concentrations with observed and simulated desalinization (Figure 3b) is by means of some differential retention mechanism of nitrate within the brine network as suggested for ammonium in Antarctic sea ice that appears to be efficiently adsorbed onto organic matter, with likely consequences to its mobility and availability [*Fripiat et al.*, 2017]. Thus, the comparatively high observed bulk concentrations of nitrate in the RL remain to be explained.

Silicic acid concentrations at bottom ice drop to nearly zero in the RL simulations a short while after the onset of algal growth, around 19 May (Figures 6a–6c). The strong effect of biological uptake on silicic acid is emphasized by the differences between Figures 4e and 4f. The limiting effect of silicon (Figure 5d) stopped algal growth in the RL simulations, even after reducing the effect of the silicon limiting parameters (simulations RL_Sim_2, RL_Sim_3, and RL_Sim_5; Table 1). It can be argued that the increase in Chl *a* standing stock shown by the empirical data (Figure 6d) does not support the determining role of silicic acid in stopping the bloom. It is hard to explain the contradiction between simulated and observed data, considering the model parameter uncertainties and also the large variability of empirical data. The results presented in *Olsen et al.* [2017] suggest that observed cell abundances in the RL cannot be explained solely by local growth, emphasizing the importance of seeding mechanisms. Therefore, it is important to study seeding and its relationship with some physical drivers for proper inclusion in ice algal models. The claim about silicon limitation is consistent with the reported diatom dominance in the RL [*Olsen et al.*, 2017] and with the relatively high nitrate: silicic acid ratios in the water and in the ice, during the first half of the simulation period (Figures 2f and 6a). The nitrate decrease in the SYI/coring site simulation is dominated by desalinization and melting, whereas the silicon decrease is dominated by biological uptake (Figures 9c and 9d and S2). In the SYI, ice algae are limited by low light levels until the end of May, and afterward, silicon becomes more limiting (Figure 10). This is consistent with the observation that during the spring, ice algae are initially limited by light and later by nutrients [*Cota et al.*, 1991; *Leu et al.*, 2015].

The approaches described in the literature to simulate water-ice nutrient exchanges are based on different diffusive or advective mechanisms. *Arrigo et al.* [1993] separated nutrient exchanges due to gravity drainage, occurring in brine channels at an assumed constant speed, from brine convection in the skeletal layer, dependent on ice growth rate through a relationship proposed by *Wakatsuchi and Ono* [1983]. In both cases, brine fluxes were used to compute nutrient exchanges as a diffusive process. *Lavoie et al.* [2005] computed nutrient exchanges across the skeletal layer with a diffusion equation. *Jin et al.* [2006, 2008] used the equation by *Wakatsuchi and Ono* [1983] to compute nutrient fluxes across the skeletal layer but in the form of an advection term. Furthermore, molecular diffusion was added as another exchange mechanism, based on a fixed diffusion coefficient. Approaches based on the existence of a skeletal layer may be limited to winter periods of ice growth when such a layer exists [*Hunke et al.*, 2015]. More recently, other authors have attempted to integrate more physically based formulations in trying to simulate brine drainage and tracer exchanges between the ice and the seawater. The main motivation of these attempts has been to properly simulate salinity due to its influence on sea ice thermal properties and its relationship with brine dynamics and nutrient supply [*Vancoppenolle et al.*, 2007]. In line with this, CICE was upgraded first with the thermohaline approach described in *Jeffery et al.* [2011] and later with the mushy layer dynamics method of *Turner et al.* [2013]. While the former is based on a mixing length diffusion approach, the latter is based on convection and both attempt to reproduce brine drainage based on vertical density instabilities. The CICE configuration used in

this study includes brine convection and molecular diffusion as mixing mechanisms. *Jeffery et al.* [2011] compared the performance of the mixing length diffusion method with enhanced molecular diffusion (EMD) and found that the former method performed better than the latter by responding to ice growth rates. When these increase, brine production also increases leading to a rise in density instability and in mixing length diffusivity, while EMD diffusivity is constant. The use of brine drainage methods parameterized as a function of vertical density instabilities makes sense regarding the physics, but possibly, there is still room for EMD to be used not as a brine transport and desalinization mechanism but as a complementary process promoting exchanges at the bottom ice that works as a function of concentration gradients even in the absence of significant brine drainage. Ideally, diffusivity should be parameterized as a function of current shear in the same way as used to compute the heat transfer coefficient in the CICE model.

Empirical and model data synthetized in Figures 6b and 8d suggest that the bloom took place a few days later in the RL than it did in the SYI. This delay may be explained by the time needed for algae to recruit from the ocean to the RL and reach a standing stock large enough to produce a bloom, whereas such a stock, probably of overwintering algae, was available at the upper ice layers of the SYI at the beginning of the simulated period [*Olsen et al.*, 2017]. The steady increase in observed Chl *a* standing stocks that lasted until the beginning of June, after some melting took place, was unexpected, since other studies in the Arctic have suggested that after melting, there is a rapid flushing of ice algae, with Chl *a* concentrations dropping rapidly to near zero values [*Leu et al.*, 2015]. Therefore, it may be hypothesized that ice algae may cope with some melting still being able to increase their biomasses, possibly taking advantage of more light availability with decreasing ice and snow thickness. This suggests that the CICE parameterization that takes into account the motility of diatoms (see section 2.2) is consistent with observations. In fact, preliminary simulations without considering ice algal motility lead to the loss of Chl *a* toward the end of the simulations in contrast with observations. In spite of this, the model calculated a steady increase of the ice algae standing stock until the beginning of June only for the SYI—silicon limitation became the dominant factor in the RL simulation. Considering all simulations, model average vertically integrated NPP was in the ranges 0.5–1.0 and 1.0–1.8 mg C m^{-2} d^{-1} for the RL and SYI, respectively. These values are well within ranges reported in the literature [e.g., *Mock and Gradinger*, 1999].

Model performance regarding vertically averaged Chl *a* concentrations and Chl *a* standing stocks improved by lowering the Si:N ratio and reducing the half saturation constant for silicon uptake (Tables 1 and 2). Both for the RL and for the SYI, these parameter changes lead to quality levels between good and excellent. In what concerns vertically resolved Chl *a* concentrations, model performance was much poorer.

5.4. Ice Algal Motility

The "deterministic" algorithm implemented in SYI_Sim_3 and SYI_Sim_4 resulted in vertical Chl *a* profiles with more than one maxima (Figure 9h) similar to patterns shown in empirical data (Figure 9e) and reported in more detail in *Olsen et al.* [2017]. Algal motion was driven by an optimization search at a realistic speed, and migration toward the bottom led to access to higher nitrogen concentrations. However, this is a good strategy for part of the algae but not for all of them, depending on environmental gradients in their proximity. Therefore, some algae remained or moved closer to the ice top, where silicon and light limitations are milder (Figure 10d). The direction of the motion depends on which factors are more limiting at various depths in the ice. Figures 10c and 10d show that both nitrogen and silicon limitation are milder at ice bottom and top. In the former case this is due to exchanges between the ice and the sea, and in the latter case, it is explained by the very high brine concentrations (Figure S3) and their low utilization due to very low Chl *a* concentrations at the top layers, for most of the simulation period (Figure 9h).

Previous authors identified the need of including behavior in ice algal growth models [*Aumack et al.*, 2014] as a way to properly reproduce some of their dynamic responses to environmental variability, with emphasis on adjustments to light intensity to reduce limitation by low or high light (photoinhibition). Most likely, light intensity cannot be the sole variable explaining the direction of algal motion. Otherwise, ice algae would tend to concentrate closer to the ice top under thick ice and snow and only one Chl *a* maximum would be expected, unless different taxonomic groups responded quite differently to light. The obtained results suggest a hypothesis that may be experimentally accessed: "ice algae optimize their vertical position in the ice as a function of several potentially limiting factors." Testing this hypothesis may help in explaining the mechanisms driving ice algal motion and allowing the improvement of ice algal models.

5.5. Final Remarks

It is well established that the parameters controlling the relationship between primary production and irradiance change at variable time scales as result of adjustments of the photosynthetic apparatus to different light regimes. Chl *a* per cell may increase 5 to 10 times as irradiance decreases, alleviating light limitation at low irradiances [*Falkowski and Wirick*, 1981; *Falkowski and Raven*, 1997]. If this plasticity is not taken into account in the production-irradiance relationship of ice algal models, it is more difficult to properly reproduce algal growth under strikingly different light environments such as the refrozen lead with thin snow cover and thicker ice with thick snow encountered during this study. Moreover, this plasticity has consequences for the total amount of chlorophyll and the comparisons between observed and simulated surrogates of ice algal biomass. This is why some ecosystem models treat Chl *a* as a prognostic variable [e.g., *Fennel et al.*, 2006; *Vichi et al.*, 2007]. In line with the above reasoning, we note that the highest Chl *a* values observed under SYI correspond to some of the lowest observed particulate organic carbon (POC) and PON values (data not shown). In spite of the fact that POC/PON includes not only ice algae, it is tempting to speculate that the reason for the apparent discrepancy could be a high Chl *a* content per cell as a response to low irradiances.

Whatever tuning of ice algal physiological parameters may be attempted, it is difficult to properly reproduce growth under very different light environments without considering the effects of light acclimation. In fact, while for the RL one would expect a reduction in photosynthetic efficiency as a result of acclimation to high light, the opposite would make more sense for the thick ice and snow under which light levels are very low (Figure 8a). All things considered, we hypothesize that the CICE biogeochemical submodel would benefit from the incorporation of Chl *a* dynamics following *Fennel et al.* [2006] and *Vichi et al.* [2007].

This work does not include a thorough sensitivity analysis, which generally implies changing each parameter at a time, running the model and comparing the results with a reference simulation. However, as already noted by *Urrego-Blanco et al.* [2016], such an approach cannot identify interactions among parameters and assumes linearity and additivity. The same authors used a global variance approach with Sobol sequences to efficiently sample the parameter space of the CICE model. This method provided a thorough analysis of the CICE model sensitivity to physical parameters [*Urrego-Blanco et al.*, 2016]. A comparative analysis including the biogeochemical parameters is beyond the scope of the present work but would certainly shed light over the complex synergies among these parameters and their interactions with physical processes.

This study is a relatively thorough evaluation of a sea ice model at the floe scale, covering physical, chemical, and biological variables and using a comprehensive data set of forcing functions with high temporal resolution. In spite of that, there are limitations in the available data not allowing for an exhaustive analysis of model performance with the same degree of detail for all variables and for the different types of ice. These limitations include the low frequency for some observations, such as vertical salinity profiles in SYI and sea ice bulk nutrient concentrations in the RL, and the lack of replication of SYI data. This last limitation makes it difficult to evaluate how much of the Chl *a* variability observed over the simulated period (Figure 9e) is due to temporal or to spatial trends. Overall, model performance is poor for vertically resolved Chl *a* concentrations and between good and excellent for vertically averaged Chl *a* concentrations and Chl *a* standing stocks, depending on some parameter tuning. In what concerns ice thickness and vertically averaged salinity the model does reasonably well, with a relatively low bias. The best performance is for vertically resolved sea ice temperature showing that model thermodynamics performs very well.

The obtained results suggest fundamental differences between pack ice with a thick snow cover and refrozen leads in what concerns ice algal bloom dynamics. In the former, blooms have the following characteristics (see also *Olsen et al.* [2017]): (i) sustained for a longer period due to a higher nutrient "buffer" and a strong light limitation; (ii) possibly seeded from overwintering ice algae at the upper ice layers; (iii) with possibly several Chl *a* maximum along the vertical, likely resulting from algal motion as a function of limiting factor gradients; and (iv) higher vertically integrated NPP as a result of larger standing stocks of ice algae. In the latter, blooms are characterized by (i) rapid nutrient exhaustion, as a result of fast nonlight limited algal growth; (ii) total dependence on recruitment from the water column; and (iii) only one Chl *a* maximum located at bottom ice to overcome nutrient limitation.

Over the last decades there has been an increase in drift speeds and sea ice deformation implying stronger fracturing and more lead opening [*Rampal et al.*, 2009; *Kwok et al.*, 2013; *Itkin et al.*, 2017]. If these trends continue, it is likely that the frequency of refrozen leads will increase, impacting Arctic Ocean ecology.

Phytoplankton blooms beneath snow-covered ice might become more frequent and widespread in the future Arctic Ocean with more lead formation due to thinner and more dynamic ice cover [*Assmy et al.*, 2017]. The results presented in this work suggest that higher maximal ice algal growth rates in thin ice lead to not only more pronounced blooms (sharper bloom peak) but also earlier nutrient exhaustion in the high-biomass ice bottom layer (shorter blooms), which might result in a reduction in ice algal vertically integrated NPP and standing stocks (per m^2) in thin ice relative to what is observed in thicker ice, with an overwintering standing stock of ice algae. This would lead to important effects on marine food webs and carbon sequestration.

6. Conclusions

Considering the questions behind this study and results obtained, we emphasize the following points: (i) it is possible to simulate reasonably well sea ice thickness and bulk salinity and to simulate very well vertically resolved temperature at time scales of a few weeks, with minimum parameter tuning when a complete forcing data set of atmospheric and oceanographic conditions is available; (ii) model accuracy is good for vertically averaged Chl *a* concentrations and Chl *a* standing stocks depending on parameter tuning and poor for vertically resolved Chl *a* concentrations; (iii) improving current knowledge about the mechanisms of nutrient exchanges at the sea ice-ocean interface, ice algal recruitment, and motion within the brine matrix is critical to improve sea ice biogeochemical modeling; (iv) ice algae may bloom despite some degree of bottom melting, presumably avoiding flushing due to their motility; (v) ice algal motility driven by gradients in limiting factors is a plausible mechanism to explain their vertical distribution; (vi) different ice algal bloom and NPP patterns were identified in the ice types studied, suggesting that ice algal growth rates may be higher in RLs than in thicker SYI with a thick snow cover but vertically integrated NPP and biomasses are larger in the latter than in the former; and (vii) these differences combined with the expected increasing trend in the frequency of refrozen leads may impact Arctic Ocean primary production with possible effects on marine food webs and carbon sequestration.

Acknowledgments

This work has been supported by the Norwegian Polar Institute's Centre for Ice, Climate, and Ecosystems (ICE), through the N-ICE project, by the Norges Forskningsråd, through projects "Boom or Bust" (244646) and "STASIS" (221961/F20), by the Ministries of Foreign Affairs and Climate and Environment of Norway, through project "Interdisciplinary study of Arctic sea ice changes and impacts for the society" (project ID Arctic), by the Fram Centre Arctic Ocean flagship project "Ecosystem modelling of the Arctic Ocean around Svalbard (ArctisMod)," and by the Norwegian Metacenter for Computational Science application "NN9300K—Ecosystem modeling of the Arctic Ocean around Svalbard." Algot K. Peterson was supported by the Research Council of Norway, through the project 229786, and the Centre for Climate Dynamics at the Bjerknes Centre through grant BASIC: Boundary Layers in the Arctic Atmosphere, Seas and Ice Dynamics. We thank the captains, crews, engineers, and science parties during N-ICE2015 for their help in making this study possible. Special thanks are due to the students that helped during field work: Jens Dujardin, Maja Hatlebakk, and Marthe Sandbu. The data used in this study are publicly available at the Norwegian Polar Data Centre: https://data.npolar.no/ under the keyword N-ICE2015. We thank the U. S. Department of Energy's (DOE) Earth System Modeling Program for allowing the use of this version of the CICE model, which includes updated biogeochemistry parameterizations within a "column package" developed as part of the Accelerated Climate Model for Energy (ACME) project. Tuning and model validation work performed under the DOE Regional and Global Climate Modeling Program also contributed to these results.

References

Allen, J. I., J. T. Holt, J. Blackford, and R. Proctor (2007), Error quantification of a high resolution coupled hydrodynamic-ecosystem coastal-ocean model: Part 2. Chlorophyll-a, nutrients and SPM, *J. Mar. Syst.*, *68*, 381–404.

Ardyna, M., M. Babin, M. Gosselin, E. Devred, L. Rainville, and J.-É. Tremblay (2014), Recent Arctic Ocean sea ice loss triggers novel fall phytoplankton blooms, *Geophys. Res. Lett.*, *41*, 6207–6212, doi:10.1002/2014GL061047.

Arrigo, K. R., and C. W. Sullivan (1994), A high resolution bio-optical model of microalgal growth: Tests using sea-ice algal community time-series data, *Limnol. Oceanogr.*, *39*, 609–631.

Arrigo, K. R., J. N. Kremer, and C. W. Sullivan (1993), A simulated Antarctic fast ice ecosystem, *J. Geophys. Res.*, *98*, 6926–6946.

Arrigo, K. R., and G. L. van Dijken (2015), Continued increases in Arctic Ocean primary production, *Prog. Oceanogr.*, *136*, 60–70.

Assmy, P., et al. (2016), N-ICE2015 water column biogeochemistry [data set], Norwegian Polar Institute. [Available at https://doi.org/10.21334/npolar.2016.3ebb7f64.]

Assmy, P., et al. (2017), Leads in Arctic pack ice enable early phytoplankton blooms below snow covered sea ice, *Sci. Rep.*, *7*, 40850, doi:10.1038/srep40850.

Aumack, C. F., A. R. Juhl, and C. Krembs (2014), Diatom vertical migration within land-fast Arctic sea ice, *J. Marine Sys.*, *139*, 496–504.

Barber, D. G., et al. (2015), Selected physical, biological and biogeochemical implications of a rapidly changing Arctic marginal ice zone, *Prog. Oceanogr.*, *139*, 122–150.

Brzrezinzki, M. A. (1985), The Si:C:N ratio of marine diatoms: Interspecific variability and the effect of some environmental variables, *J. Phycol.*, *21*, 347–357.

Cohen, L., S. R. Hudson, V. P. Walden, and M. A. Granskog (2017), Meteorological conditions in a thinner Arctic sea ICE regime from winter through spring during the Norwegian young sea ICE expedition (N-ICE2015), *J. Geophys. Res. Atmos.*, *122*, doi:10.1002/2016JD026034.

Convention for the Protection of the Marine Environment of the North-East Atlantic (OSPAR) Commission (1998), Report of the modelling workshop on eutrophication issues, *OSPAR Rep.*, 86 pp., Den Haag, Netherlands, 5–8 Nov. 1996.

Cota, G. F., L. Legendre, M. Gosselin, and R. G. Ingram (1991), Ecology of bottom ice algae: III. Comparative physiology, *J. Mar. Syst.*, *2*, 297–315.

Cottier, F., H. Eicken, and P. Wadhams (1999), Linkages between salinity and brine channel distribution in young sea ice, *J. Geophys. Res.*, *104*, 15,859–15,871.

Döscher, R., T. Vihma, and E. Maksimovich (2014), Recent advances in understanding the Arctic climate system state and change from a sea ice perspective: A review, *Atmos. Chem. Phys.*, *14*, 13,571–13,600.

Duarte, P., P. Assmy, H. Hop, G. Spreen, S. Gerland, and S. R. Hudson (2015), The importance of vertical resolution in sea ice algae production models, *J. Mar. Syst.*, *145*, 69–90.

Elliott, S., C. Deal, G. Humphries, E. Hunke, N. Jeffery, M. Jin, M. Levasseur, and J. Stefels (2012), Pan-Arctic simulation of coupled nutrient-sulfur cycling due to sea ice biology: Preliminary results, *J. Geophys. Res.*, *117*, G01016, doi:10.1029/2011JG001649.

Falkowski, P. G., and J. A. Raven (1997), *Aquatic Photosynthesis*, 375 pp., Blackwell Sci., London.

Falkowski, P. G., and C. D. Wirick (1981), A simulation model of the effects of vertical mixing on primary productivity, *Matrix Biol.*, *65*, 69–75.

Feltham, D. L., N. Untersteiner, J. S. Wettlaufer, and M. G. Worster (2006), Sea ice is a mushy layer, *Geophys. Res. Lett.*, *33*, L14501, doi:10.1029/2006GL026290.

Fennel, K., J. Wilkin, J. Levin, J. Moisan, J. O'Reilly, and D. Haidvogel (2006), Nitrogen cycling in the Middle Atlantic Bight: Results from a three-dimensional model and implications for the North Atlantic nitrogen budget, *Global Biogeochem. Cycles*, *20*, GB3007, doi:10.1029/2005GB002456.

Fripiat, F., et al. (2017), Macro-nutrient concentrations in Antarctic pack ice: Overall patterns and overlooked processes, *Elem. Sci. Anth.*, *5*, 13, doi:10.1525/elementa.217.

Gerland, S., M. A. Granskog, J. King, and A. Rösel (2017), N-ICE2015 ICE core physics: Temperature, salinity and density [data set], Norwegian Polar Institute. [Available at https://doi.org/10.21334/npolar.2017.c3db82e3.]

Girard-Ardhuin, F., and R. Ezraty (2012), Enhanced Arctic sea ice drift estimation merging 649 radiometer and scatterometer data, *IEEE Trans. Geosci. Remote Sens.*, *650*(50), 2639–2648.

Granskog, M. A., P. Assmy, S. Gerland, G. Spreen, H. Steen, and L. H. Smedsrud (2016), Arctic research on thin ice: Consequences of Arctic sea ice loss, *Eos. Trans. AGU*, *97*, 22–26, doi:10.1029/2016EO044097.

Granskog, M. A., A. Rösel, P. A. Dodd, D. Divine, S. Gerland, T. Martma, and M. J. Leng (2017), Snow contribution to first-year and second-year Arctic sea ice mass balance north of Svalbard, *J. Geophys. Res. Oceans*, *122*, 2539–2549, doi:10.1002/2016JC012398.

Grasshoff, K. (1965), On the automatic determination of phosphate, silicate and fluoride in seawater, ICES Hydrogr. Comm. Rep. 129.

Hegseth, E. N. (1992), Sub-ice algal assemblages of the Barents Sea: Species composition, chemical composition, and growth rates, *Polar. Biol.*, *12*, 485–496.

Hudson, S. R., M. A. Granskog, A. Sundfjord, A. Randelhoff, A. H. H. Renner, and D. V. Divine (2013), Energy budget of first-year Arctic sea ice in advanced stages of melt, *Geophys. Res. Lett.*, *40*, 2679–2683, doi:10.1002/grl.50517.

Hudson, S. R., L. Cohen and, V. Walden (2015), N-ICE2015 surface meteorology [data set], Norwegian Polar Institute. [Available at https://doi.org/10.21334/npolar.2015.056a61d1.]

Hudson, S. R., L. Cohen and, V. P. Walden (2016), N-ICE2015 surface broadband radiation data [data set]. Norwegian Polar Institute. [Available at https://doi.org/10.21334/npolar.2016.a89cb766.]

Hunke, E. C., W. H. Lipscomb, A. K. Turner, N. Jeffery, and S. Elliot (2015), CICE: The Los Alamos sea ice model documentation and user's manual version 5.1. *Tech. Rep., LA-CC-06-012*, Los Alamos National Laboratory, Los Alamos, N. M.

Huwald, H., L.-B. Tremblay, and H. Blatter (2005), A multilayer sigma-coordinate thermodynamic sea ice model: Validation against surface heat budget of the Arctic Ocean (SHEBA)//Sea Ice Model Intercomparison Project Part 2 (SIMIP2) data, *J. Geophys. Res.*, *110*, C05010, doi:10.1029/2004JC002328.

Itkin, P., et al. (2015), N-ICE2015 buoy data [data set]. Norwegian Polar Institute. [Available at https://doi.org/10.21334/npolar.2015.6ed9a8ca.]

Itkin, P., et al. (2017), Thin ICE and storms: Sea ice deformation from buoy 1 arrays deployed during N-ICE2015, *J. Geophys. Res. Oceans*, *122*, doi:10.1002/2016JC012403.

Jackson, K., J. Wilkinson, T. Maksym, J. Beckers, C. Haas, D. Meldrum, and D. Mackenzie (2013), A novel and low cost sea ice mass balance buoy, *J. Atmos. Oceanic Tech.*, *30*, 2676–2688, doi:10.1175/JTECH-D-13-00058.1.

Jeffery, N., and E. C. Hunke (2014), Modeling the winter-spring transition of first-year ice in the western Weddell Sea, *J. Geophys. Res. Oceans*, *119*, 5891–5920, doi:10.1002/2013JC009634.

Jeffery, N., E. C. Hunke, and S. M. Elliott (2011), Modeling the transport of passive tracers in sea ice, *J. Geophys. Res.*, *116*, C07020, doi:10.1029/2010JC006527.

Jeffery, N., S. Elliott, E. C. Hunke, W. H. Lipscomb, and A. K. Turner (2016), Biogeochemistry of CICE: The Los Alamos Sea Ice Model, Documentation and User's Manual. Zbgc_colpkg modifications to Version 5, Los Alamos National Laboratory, Los Alamos, N. M.

Ji, R., M. Jin, and Ø. Varpe (2013), Sea ice phenology and timing of primary production pulses in the Arctic Ocean, *Global Change Biol.*, *19*, 734–741, doi:10.1111/gcb.12074.

Jin, M., C. J. Deal, J. Wang, K.-H. Shin, N. Tanaka, T. E. Whitledge, S. H. Lee, and R. R. Gradinger (2006), Controls of the landfast ice-ocean ecosystem offshore Barrow, Alaska, *Ann. Glaciol.*, *44*, 63–72.

Jin, M., C. Deal, and W. Jia (2008), A coupled ice-ocean ecosystem model doe 1-D and 3-D applications in the Bering and Chukchi Seas, *Chinese J. Pol. Sci.*, *19*, 218–229.

Jin, M., C. Deal, S. H. Lee, S. Elliot, E. Hunke, M. Maltrud, and N. Jeffery (2012), Investigation of Arctic sea ice and ocean primary production for the period 1992–2007 using a 3-D global ice-ocean ecosystem model, *Deep Sea Res., Part II*, *81-84*, 28–35.

Jørgensen, S. E., S. N. Nielsen, and L. A. Jørgensen (1991), *Handbook of Ecological Parameters and Ecotoxicology*, 1263 pp., Elsevier, Amsterdam.

Kauko, H. M., et al. (2017), Windows in Arctic sea ice: Light transmission and ice algal optical properties in a refrozen lead, *J. Geophys. Res. Biogeosci.*, *122*, doi:10.1002/2016JG003626.

Kwok, R., G. Spreen, and S. Pang (2013), Arctic sea ice circulation and drift speed: Decadal trends and ocean currents, *J. Geophys. Res. Oceans*, *118*, 2408–2425, doi:10.1002/jgrc.20191.

Lavoie, D., K. Denman, and C. Michel (2005), Modeling ice algal growth and decline in a seasonally ice-covered region of the Arctic (Resolute Passage, Canadian Archipelago), *J. Geophys. Res.*, *110*, C11009, doi:10.1029/2005JC002922.

Leu, E., C. J. Mundy, P. Assmy, K. Campbell, T. M. Gabrielsen, M. Gosselin, T. Juul-Pedersen, and R. Gradinger (2015), Arctic spring awakening—Steering principles behind the phenology of vernal ice algal blooms, *Prog. Oceanogr.*, *139*, 151–170.

Maréchal, D. (2004), A soil-based approach to rainfall-runoff modelling in ungauged catchments for England and Wales, PhD thesis, Cranfield Univ.

Maslanik, J., J. Stroeve, C. Fowler, and W. Emery (2011), Distribution and trends in Arctic sea ice age through spring 2011, *Geophys. Res. Lett.*, *38*, L13502, doi:10.1029/2011GL047735.

Melnikov, I. A., E. G. Kolosova, H. E. Welch, and L. S. Zhitina (2002), Sea ice biological communities and nutrient dynamics in the Canada Basin of the Arctic Ocean, *Deep Sea Res., Part I*, *49*, 1623–1649.

Meyer, A., et al. (2017a), Winter to summer hydrographic and current observations in the Arctic Ocean north of Svalbard, *J. Geophys. Res. Oceans*, doi:10.1002/2016JC012391.

Meyer, A., I. Fer, A. Sundfjord, and A. K. Peterson (2017b), Mixing rates and vertical heat fluxes north of Svalbard from Arctic winter to spring, *J. Geophys. Res. Oceans.*, *122*, doi:10.1002/2016JC012441.

Mock, T., and R. Gradinger (1999), Determination of ice-algal production with a new in situ incubation technique, *Mar. Ecol. Prog. Ser.*, *177*, 15–26.

Nash, J. E., and J. V. Sutcliffe (1970), River flow forecasting through conceptual models. Part I e a discussion of principles, *J. Hydrol.*, *10*, 282–290.

Nelson, D. M., and P. Tréguer (1992), Role of silicon as a limiting nutrient to Antarctic diatoms: Evidence from kinetic studies in the Ross Sea ice-edge zone, *Mar. Ecol. Prog. Ser.*, *80*, 255–264.

Notz, D. (2005), Thermodynamic and fluid-dynamical processes in sea ice, PhD thesis, Univ. of Cambridge, Cambridge, U. K.
Notz, D., and M. G. Worster (2008), In situ measurements of the evolution of young sea ice, *J. Geophys. Res.*, *113*, C03001, doi:10.1029/2007JC004333.
Olsen, L. M., et al. (2017), The role of multiyear ice in the seeding of ice-algae blooms in Arctic pack ice, *J. Geophys. Res. Biogeosci.*, *122*, doi:10.1002/2016JG003668.
Peterson, A. K., I. Fer, A. Randelhoff, A. Meyer, L. Håvik, L. H. Smedsrud, L. Onarheim, M. Muilwijk, A. Sundfjord, and M. G. McPhee (2016), N-ICE2015 ocean turbulent fluxes from under-ICE turbulence cluster (TIC) [data set], Norwegian Polar Institute. [Available at https://doi.org/10.21334/npolar.2016.ab29f1e2.]
Peterson, A. K., I. Fer, M. G. McPhee, and A. Randelhoff (2017), Turbulent heat and momentum fluxes in the upper ocean under Arctic sea ice, *J. Geophys. Res. Oceans*, *122*, 1439–1456, doi:10.1002/2016JC012283.
Pogson, L., B. Tremblay, D. Lavoie, C. Michel, and M. Vancoppenolle (2011), Development and validation of a one-dimensional snow-ice algae model against observations in Resolute Passage, Canadian Arctic Archipelago, *J. Geophys. Res.*, *116*, C04010, doi:10.1029/2010JC006119.
Popova, E. E., A. Yool, A. C. Coward, F. Dupont, C. Deal, S. Elliot, E. Hunke, M. Jin, M. Steele, and J. Zhang (2012), What controls primary production in the Arctic Ocean? Results from an intercomparison of five general circulation models with biogeochemistry, *J. Geophys. Res.*, *117*, C00D12, doi:10.1029/2011JC007112.
Radach, G., and A. Moll (2006), Review of three-dimensional ecological modeling related to the North Sea shelf system. Part II: Model validation and data needs, *Oceanogr. Mar. Biol. Annu. Rev.*, *44*, 1–60.
Rampal, P., J. Weiss, and D. Marsan (2009), Positive trend in the mean speed and deformation rate of Arctic sea ice, 1979–2007, *J. Geophys. Res.*, *114*, C05013, doi:10.1029/2008JC005066.
Rösel, A., et al. (2016a), N-ICE2015 total (snow and ICE) thickness data from EM31 [data set]. Norwegian Polar Institute. [Available at https://doi.org/10.21334/npolar.2016.70352512.]
Rösel, A., et al. (2016b), N-ICE2015 snow depth data with magna probe [data set], Norwegian Polar Institute. [Available at https://doi.org/10.21334/npolar.2016.3d72756d.]
Saburova, M. A., and I. G. Polikarpov (2003), Diatom activity within soft sediments: Behavioural and physiological processes, *Mar. Ecol. Prog. Ser.*, *251*, 115–126.
Sedlacek, J., J.-F. Lemieux, and L. A. Mysak (2007), The Granular Sea ice model in spherical coordinates and its application to a global climate model, *J. Clim.*, *20*, 5946–5961.
Shu, Q., Z. Song, and F. Qiao (2015), Assessment of sea ice simulations in the CMIP5 models, *Cryosphere*, *9*, 399–409.
Slagstad, D., I. H. Ellingsen, and P. Wassman (2011), Evaluating primary and secondary production in an Arctic Ocean void of summer sea ice: An experimental simulation approach, *Prog. Oceanogr.*, *90*, 117–131.
Slagstad, D., P. Wassman, and I. H. Ellingsen (2015), Physical constrains and productivity in the future Arctic Ocean, *Ocean. Front. Mar. Sci.*, *2*, 85, doi:10.3389/fmars.2015.00085.
Smith, R. E. H., J. F. Cavaletto, B. J. Eadie, and W. S. Gardner (1993), Growth and lipid composition of high Arctic ice algae during the spring bloom at resolute, northwest territories, Canada, *Mar. Ecol. Prog. Ser.*, *97*, 19–29.
Steiner, N., C. Deal, D. Lannuzel, D. Lavoie, F. Massonnet, L. A. Miller, S. Moreau, E. Popova, J. Stefels, and L. Tedesco (2016), What sea-ice biogeochemical modellers need from observers, *Elementa*, *4*, 84, doi:10.12952/journal.elementa.000084.
Taskjelle, T., S. R. Hudson, A. Pavlov, and M. A. Granskog (2016), N-ICE2015 surface and under-ICE spectral shortwave radiation data [data set], Norwegian Polar Institute. [Available at https://doi.org/10.21334/npolar.2016.9089792e.]
Taskjelle, T., M. A. Granskog, A. K. Pavlov, S. R. Hudson, and B. Hamre (2017), Effects of an Arctic under-ice bloom on solar radiant heating of the water column, *J. Geophys. Res. Oceans*, *122*, 126–138, doi:10.1002/2016JC012187.
Tedesco, L., and M. Vichi (2014), Sea ice biogeochemistry: A guide for modellers, *PLoS One*, *9*(2), e89217, doi:10.1371/journal.pone.0089217.
Turner, A. K., E. C. Hunke, and M. Bitz (2013), Two modes of sea-ice gravity drainage: A parameterization for large-scale modeling, *J. Geophys. Res. Oceans*, *118*, 2279–2294, doi:10.1002/jgrc.20171.
Urrego-Blanco, J. R., N. M. Urban, E. C. Hunke, A. K. Turner, and N. Jeffery (2016), Uncertainty quantification and global sensitivity analysis of the Los Alamos Sea Ice Model, *J. Geophys. Res. Oceans*, *121*, 2709–2732, doi:10.1002/2015JC011558.
Vancoppenolle, M., C. M. Bitz, and T. Fichefet (2007), Summer landfast sea ice desalination at Point Barrow, Alaska: Modeling and observations, *J. Geophys. Res.*, *112*, C04022, doi:10.1029/2006JC003493.
Vancoppenolle, M., T. Fichefet, H. Goosse, S. Bouillon, G. Madec, and M. A. M. Maqueda (2009), Simulating the mass balance and salinity of Arctic and Antarctic sea ice.1. Model description and validation, *Ocean Model.*, *27*, 33–53.
Vancoppenolle, M., L. Bopp, G. Madec, J. Dunne, T. Ilyina, P. R. Halloran, and N. Steiner (2013a), Future Arctic Ocean primary productivity from CMIP5 simulations: Uncertain outcome, but consistent mechanisms, *Global Biogeochem. Cycles*, *27*, 605–619, doi:10.1002/gbc.20055.
Vancoppenolle, M., et al. (2013b), Role of sea ice in global biogeochemical cycles: Emerging views and challenges, *Quat. Sci. Rev.*, *79*, 207–230.
Vichi, M., N. Pinardi, and S. Masina (2007), A generalized model of pelagic biogeochemistry for the global ocean ecosystem. Part I: Theory, *J. Mar. Syst.*, *64*, 89–109.
Wakatsuchi, M., and N. Ono (1983), Measurements of salinity and volume of brine excluded from growing sea ice, *J. Geophys. Res.*, *88*, 2943–2951.
Wang, C., B. Cheng, K. Wang, S. Gerland, and O. Pavlova (2015), Modeling snow ice and superimposed ice on landfast sea ice in Kongsfjorden, Svalbard, *Polar Res.*, *34*, 20828, doi:10.3402/polar.v34.20828.